Multiplicity dependence of $\boldsymbol{\sigma_{\psi(2S)}/\sigma_{J/\psi}}$ in $\boldsymbol{p}$Pb collisions at $\boldsymbol{\sqrt{s_{NN}} = 8.16}$ TeV

Xianglei Zhu, Youen Kang, Li Xu, Chenzhi Dong.

Tsinghua University

Abstract

Using a data sample with an integrated luminosity of 13.6 nb^{-1} for pPb collisions and 20.8 nb^{-1} for Pbp collisions collected by the LHCb detector in the LHC operations in 2016, ratio of production cross section of $\psi(2S)$ over J/ψ as a function of multiplicity was measured at a centre-of-mass energy $\sqrt{s_{NN}} = 8.16$ TeV. A multiplicity-dependent modification of the ratio has been observed for prompt mesons in pPb collisions when there is an overlap between the rapidity ranges where the multiplicity and the charmonia production are measured. No evident modification of same significance for that of non-prompt component is observed. In Pbp collisions, there is a overall reduction in the ratio compared to that in pPb collisions, but no obvious decreasing trend on the ratio is observed for both prompt and non-prompt mesons. The ratio as a function of multiplicity is compared to co-mover model. The ratio measured in pPb and Pbp collisions are compared to other measurements in different collision systems, which shows a good agreement.

Contents

1   Introduction

Quark-Gluon Plasma (QGP) [1] is a form of matter which has extreme high temperature and density. Within QGP, quarks and gluons are deconfined and become asymptotically free. It is expected to exist in the early stage of universe, which is shortly after the Big Bang. A possible way to study QGP is in heavy-ion collisions. With ultra-relevatistic collision energy, heavy-ion collisions provide a extremely hot and dense environment where QGP may be produced. Quarkonium production in hadronic collisions is a good probe for QGP as the production time is significantly shorter than the formation of QGP.

Heavy quarks experience the whole time evolution of collisions and therefore, the production of quarkonium is infected by initial-state effects like nuclear parton distribution function (nPDFs) for Pb and parton distribution function for proton [2], and energy loss from multi-particle scattering [3]. These effects may result in the enhancement or suppression on quarkonium production. When considering the excite-to-ground production ratio of quarkonium, these initial-state effects are expected to be canceled. While the exctied state of charmonia ($\psi(2S)$) and bottomonia ($\Upsilon(2S)$, $\Upsilon(3S)$) are preferentially suppressed than their ground state J/ψ and $\Upsilon(1S)$ [4–6], which can not be explained by initial-state effects. It suggests that additional, final-state effects need to be taken into consideration such as interacting with co-moving particles [7].

Measurement of J/ψ and $\psi(2S)$ production as a function of centrality in pPb collisions at $\sqrt{s_{NN}} = 8.16$ TeV [8] suggests that $\psi(2S)$ is more sensitive to final-state interactions. The nuclear modification of $\psi(2S)$ is significantly lower than that of J/ψ except in the lowest and highest multiplicity class. CMS collaboration measured the event activity dependence of $\Upsilon(nS)$ production in $\sqrt{s_{NN}} = 5.02$ TeV pPb and $\sqrt{s} = 2.76$ TeV pp collisions [9], where the cross section ratios $\Upsilon(2S)/\Upsilon(1S)$ and $\Upsilon(3S)/\Upsilon(1S)$ decrease with multiplicities. The measurements come to an agreement that,excited-state quarkonia are more sensitive to final-state effects, and final-state effects show dependence on charged particle multiplicity.

Besides, signatures revealing the presence of QGP are observed in high-multiplicity pp and pPb collisions, such as strangeness enhancement [10], a high degree of collectivity flow [11] and long-range near- and away-side ridges in twoparticle azimuthal correlations [12–15]. The possible existence of QGP could infect the excite-to-ground ratio of quarkonia. Excited energy level quarkonia will dissociate first in QGP due to the loose bound compared to ground level. Therefore, multiplicity-dependent studies also serve as a testing ground for QGP-like behaviours in small systems.

The analysis proceeds as follows, samples of J/ψ and $\psi(2S)$ are selected from 8.16 TeV pPb collisions data collected in 2016, by fitting the invariant mass spectrum of oppositely charged muons. Prompt and non-prompt components are separated by fitting the pseudo proper-time in multiple bins of multiplicity. Then the yields are corrected by the efficiencies from different sources. Then the ratio of production is calculated in each multiplicity bin to come to a final result. Three variables, PVNTRACKS, nForwardTracks and nBackwardTracks, are used as proxy for the multiplicity of the pPb collisions. PVNTRACKS is the number of tracks used to reconstruct the primary vertex, and nBackTracks is the number of tracks in the backward directions. PVNTRACKS is the global multiplicity of the pp collisions while nForwardTracks is the multiplicity measured in the same phase space as the two charmonia. Some correlations between the ratio and nForwardTracks can appear and due to that, the use of nBackTracks, allows to reduce

2

83 this effect.

2 Data sets

2.1 Data samples

86 The data used in this analysis was recorded during the Heavy Ion run 2016, between Nov.
87 18th and Nov. 25th for the pPb configurtion and between Nov. 26th and Dec. 4th for
88 the Pbp configuration, both at a center-of-mass energy of 8.16 TeV. The total recorded
89 luminosity is of 13.6 ± 0.3nb^{-1} for pPb and 20.8 ± 0.5nb^{-1} for Pbp. The magnet polarity
90 was always DOWN throughout the whole period. The list of good runs are listed in
91 Table 1. The bookkeeping paths for data samples are as follows.

92 • pPb   /LHCb/Protonion16/Beam6500GeV-VeloClosed-MagDown/Real
93   Data/Turbo03pLead/94000000/TURBO.MDST

94 • Pbp /LHCb/Ionproton16/Beam6500GeV-VeloClosed-MagDown/Real
95   Data/Turbo03pLead/94000000/TURBO.MDST

2.2 Monte Carlo samples

97 The efficiency of the various steps in the analysis is estimated using samples of fully
98 simulated events using the standard LHCb simulation software tools as the ones used for
99 data. The simulation is done in two successive steps, first a generation phase based on
100 several external tools such as event generators, and second a simulation phase based on
101 the Geant4 package [16, 17]. The simulation phase is the same as the one used for the
102 simulation of pp events within LHCb and is described in Ref. [18] while the geneartion
103 phase is specific to the heavy ion analysis. And in this analysis, we use a multiplicity-fix
104 Monte Carlo sample which has a multiplicity distribution more closed to the data sample.
105 The version of the software for the simulation is Sim09l and the bookkeeping paths are as
106 follows.

107 • pPb   /MC/2016/pPb-Beam6500GeV-2560GeV-2016-MagDown-Fix1-
108   Epos/Sim09l/Trig0x61421621/Reco16pLead/Turbo03/eventType/DST

109 • Pbp /MC/2016/Pbp-Beam2560GeV-6500GeV-2016-MagDown-Fix1-
110   Epos/Sim09l/Trig0x61421621/Reco16pLead/Turbo03/eventType/DST

111 In the paths, eventType is 24142001 for J/ψ and 28142001 for $\psi(2S)$. Minimum bias
112 samples of pPb and Pbp collisions are generated using the Epos event generator, using
113 the LHC model [19]. This generator is interfaced with the Gauss simulation software
114 via the CRMC (Cosmic Ray Monte Carlo) interface library. All short lived particles are
115 decayed with the EvtGen decay package [20], similarly to what is done for pp simulation
116 in LHCb. Radiative QED corrections to the decays containing charged particles in the
117 final state are applied with the Photos package [21] and is particularly important for
118 J/ψ and $\psi(2S)$ ro dimuon decays. Since the instantaneous luminosity of the collisions
119 recorded by the experiment in the various heavy ion configuration is low, no pile-up is
120 generated, and events contain only one interaction. Signal samples of $J/\psi \to \mu^+\mu^-$ and

Table 1: List of good runs

pPb	
5519	186555, 186557, 186558, 186564, 186565
5520	186583, 186584, 186585, 186587, 186588, 186590
5521	186601, 186602, 186603, 186604, 186608, 186609, 186610, 186611, 186612, 186613
5522	186614, 186615, 186616, 186626, 186628, 186629, 186631, 186632, 186633, 186634, 186635, 186636, 186637, 186638, 186639
5523	186647, 186650, 186651, 186652, 186653, 186654, 186655, 186656
5524	186670, 186673
5526	186718, 186721, 186722, 186723, 186724, 186725, 186726, 186727
5527	186735, 186737, 186739, 186740, 186741, 186744, 186745, 186746
5533	186782, 186783, 186785, 186798, 186799, 186802, 186806, 186807
5534	186818, 186819, 186823, 186824
5538	186920, 186915, 186914, 186907, 186903, 186896,186890, 186884, 186879, 186876
Pbp	
5545	186989, 186990, 186991, 186992, 186993
5546	187002, 187005, 187007
5547	187015, 187018, 187019, 187020, 187021, 187023, 187025, 187026
5549	187038, 187040, 187042, 187043, 187044, 187045, 187047, 187048, 187049, 187050, 187051
5550	187058, 187061, 187062, 187063, 187064, 187065
5552	187074, 187078, 187080, 187082, 187083, 187083, 187084, 187085, 187086
5553	187106, 187109, 187110, 187111, 187112, 187113, 187115
5554	187123, 187124, 187127, 187128, 187129
5558	187178, 187182, 187183, 187184
5559	187198, 187199, 187202, 187203, 187204
5562	187229, 187230, 187232, 187233, 187234
5563	187244, 187247, 187248, 187249, 187250, 187251, 187252, 187253, 187254, 187255
5564	187266
5565	187282, 187283, 187289, 187290, 187291, 187292
5568	187325, 187328, 187329, 187330, 187331, 187332, 187333, 187334, 187335, 187336,
1873	37, 187339, 187340
5569	187348, 187349, 187350, 187351, 187355, 187357, 187358
5570	187372, 187375, 187376, 187377, 187378, 187380, 187381
5571	187389, 187392, 187393, 187394, 187395
5573	187406, 187409, 187410

Table 2: Event type, decay and statistics of the simulation samples.

EventType	Decay chain	Number of events
24142001	pPb $J/\psi \to \mu^+\mu^-$	4.0×10^6
24142001	Pbp $J/\psi \to \mu^+\mu^-$	4.0×10^6
28142001	pPb $\psi(2S) \to \mu^+\mu^-$	4.0×10^6
28142001	Pbp $\psi(2S) \to \mu^+\mu^-$	4.0×10^6

$\psi(2S) \to \mu^+\mu^-$ are generated using an embedding technique: minimum bias events are generated using the EPOS generator, with colliding proton beams having momenta equal to the momenta per nucleon of the heavy ion beams or targets. The J/ψ ($\psi(2S)$) mesons are then extracted from these minimum bias events, discarding all other particles in the events. Their decays are forced to the signal decay modes using the EvtGen package, and the resulting decay chain is added to a single minimum bias EPOS event generated with beam parameters identical to those seen in data. All the samples are listed in Table 2.

2.3 Trigger

The trigger selections applied during the pPb and Pbp runs were close but looser than the selections used during the first month of data taking for Run 2, where the measurement of the J/ψ cross-section at 13 TeV in pp collisions was performed.

2.3.1 L0

A single L0 TCK was used throughout this run, 0x1621. The main corresponding configuration related in this analysis is given in Table 3. For this analysis, only reconstructed J/ψ and $\psi(2S)$ with one of their muons satisfying the Muon line criteria are considered (i.e. L0Muon TOS candidates). For the lines used in the analysis, no SPD multiplicity cut was applied at L0. The threshold for the muon trigger is also looser than the one used in pp collisions, which is equal to 800 MeV.

Table 3: Cuts in L0 TCK 0x1621.

Line name	Conditions
SPD	SPD multiplicity > 0
PU	Pile-Up multiplicity > 3
Muon	$p_{\mathrm{T}} > 500$ MeV
B1gas	SumEt > 4992 MeV on beam-empty crossings
B2gas	Pile-up multiplicity > 9 on empty-beam crossings

2.3.2 HLT1

Two different HLT1 configurations were used: TCK 0x11431621 for runs between 186555 and 187204, and TCK 0x11441621 for the other runs. As far as the analysis presented

5

here is concerned, these two configurations are identical (they differ only for pre-scales of
the NoBias line and of dedicated high multiplicity lines). The trigger lines used in the
analysis are given in Table 4. All candidates kept for the analysis must be TOS of the
DiMuonHighMass line.

Table 4: Cuts in HLT1 trigger line.

Variables	Cuts
Global event cut	nVelocluster < 8000
Muon p_{T}	> 300 MeV/c
Muon p	> 4 GeV/c
Track χ^2	<4
IsMuon	$=1$
$M_{\mu^+\mu^-}$	> 2.5 GeV/c

2.3.3 HLT2

Three HLT2 configurations were used: TCK 0x21421621, 0x21451621 and 0x21461621.
Here also all these TCKs are identical as far as this analysis is concerned. The selections
applied in HLT2 are described in Table 5. The lines used in the analysis are saved in the
TURBO format and the triggers candidates saved in the data RAW files are taken directly
for the final analysis. The offline processing relevant for this analysis was performed using
processing pass Turbo03pLead with DaVinci version v41r3.

Table 5: Cuts in HLT2 trigger line.

Variables	Cuts
Mass windows	150 MeV/c^2
Muon p_{T}	> 500 MeV/c
Vertex χ^2	< 25

3 Selections

3.1 Global Event Selections

Only events with less than 8000 VELO clusters are considered in this analysis, as imposed
by the trigger requirements. When measuring $\psi(2S)$-to-J/ψ production ratio, the bias
caused by this global cut is negligible since the data sample with more than 8000 VELO
clusters account for less than 0.1%. All events are also required to have exactly one
reconstructed primary vertex to avoid pile-up. For the equivalence of VELO acceptance, we
also need to restrict the z-coordinate of primary vertex. The restriction is made according
to which multiplicity variable we choose to represent the charged particle multiplicity. As
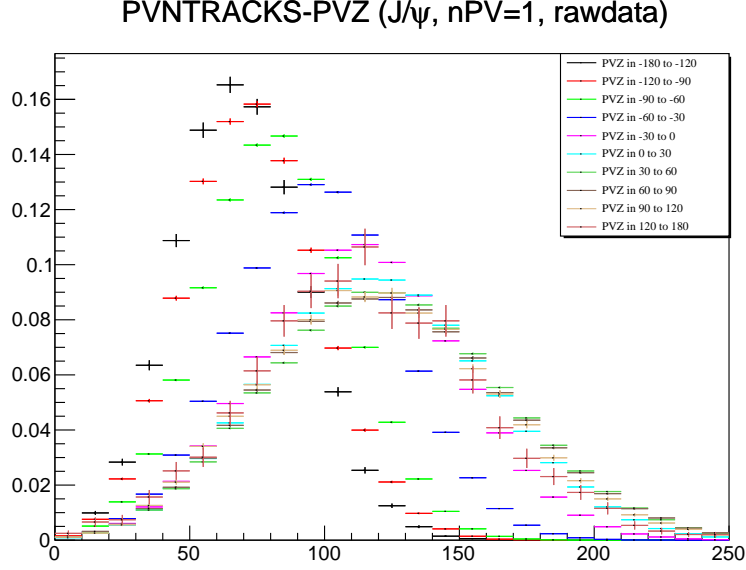an example, Figure 1 shows the PVNTRACKS distribution in different PVZ ranges. We

6

PVNTRACKS-PVZ (J/ψ, nPV=1, rawdata)

Figure 1: Distribution of PVNTRACKS in different z_{PV} ranges for J/ψ in pPb collisions.

remove the data within which the PVNTRACKS distribution is clearly deviated, which is $z_{PV} < -30$ mm in this case. The PVZ restrictions for other cases is summarized in Table 6.

Table 6: Global cuts on z_{PV}.

Configuration	Mult. Variable	z_{PV}
pPb	PVNTRACKS	[-30, 180] mm
pPb	nForwardTracks	[-180, 180] mm
pPb	nBackTracks	[-30, 180] mm
Pbp	PVNTRACKS	[-60, 180] mm
Pbp	nForwardTracks	[-180, 120] mm
Pbp	nBackTracks	[-30, 180] mm

3.2 Candidate Selection

The J/ψ and $\psi(2S)$ candidates are formed from two oppositely charged muons coming from a common vertex. Both decay modes are using same selection criteria. They are required to be TOS (Trigger On Signal) for the L0Muon and Hlt1DiMuonHighMas trigger lines, i.e. that the reconstructed candidate or its decay products are associated with a trigger object fulfilling the trigger requirements. Then the candidates used are directly the ones selected by the line Hlt2DiMuonJPsiTurbo and Hlt2DiMuonPsi2STurbo lines respectively, in the TURBO stream, without offline reconstruction. Additional cuts are applied at the analysis level. Muon tracks have to be in the geometrical acceptance of the

spectrometer ($2 < \eta < 5$) and to have $p_T > 900$ MeV/c in order to improve the signal over background ratio. Both tracks are required to have a good fit quality, $\chi^2/ndof < 3$ and a ghost probability less than 0.4. They are identified as muons by requiring ProbNN(μ) > 0.9 for both J/ψ and $\psi(2S)$. This is a harsh but appropriate PID cut since it can significantly reduce the background of high-multiplicity $\psi(2S)$ data sample. And for low-multiplicity region, it doesn't remove too much of the signals. We can therefore achieve relative low statistical uncertainties when fitting the invariant mass spectrum and pseudo decay time spectrum, since the dominant uncertainties are statistical uncertainties of $\psi(2S)$ which will be discuss later. The comparison for high- and low-multiplicity region of loose PID cut (ProbNN(μ) > 0.6) and tight PID cut (ProbNN(μ) > 0.9) can be seen in Figure 2. In addition, for both J/ψ and $\psi(2S)$, the two muons are required to form a good vertex asking the vertex fit probability Prob(χ^2) $> 0.5\%$. The $\psi(2S)$ and J/ψ candidates are required to have a mass within 120 MeV/c2 of the PDG value. All selection criteria are specified in Table 7.

Table 7: Offline selection for J/ψ and $\psi(2S)$.

Variable	Cuts
$\mu^\pm \eta$	$2 < \eta < 5$
$\mu^\pm p_T$	>900 MeV/c
ProbNNmu	>0.9
TrackGhost Prob.	<0.4
Vertex χ^2 Prob.	$> 0.5\%$
Track $\chi^2/ndof$	<3
mass window	± 120 MeV/c^2

4 Definition of observables

All observables involved in this analysis are multiplicity variables, cross-sections and ratios of cross-sections. For cross-sections and the ratios, they require efficiency corrections to event yields obtained from data. The raw event yields are extracted from a combined fit of the di-muon invariant mass and of the pseudo-proper decay time to separate the prompt and the from-b signal contributions, where the pseudo-proper decay time is defined in Eq. 1.

$$t_z = \frac{(z_{J/\psi(\psi(2S))} - z_{PV}) \times M_{J/\psi(\psi(2S))}}{p_z},$$

(1)

with $z_{J/\psi(\psi(2S))}$ the z-coordinate of the J/ψ or $\psi(2S)$ decay vertex and z_{PV} the z-coordinate of the primary vertex. **Prompt** here means produced directly at the nucleon-nucleon interaction, or via a decay of a charmonium produced directly at the interaction (such as a $\chi_c \to J/\psi\gamma$ decay). **from-b** means a charmonium coming from a B decay (either directly, or via a charmonium decay where the charmonium state is produced in a B decay). The observables of the analysis are measured separately for the prompt and from-b production components. Given the large statistics available, the observables are also computed in bin
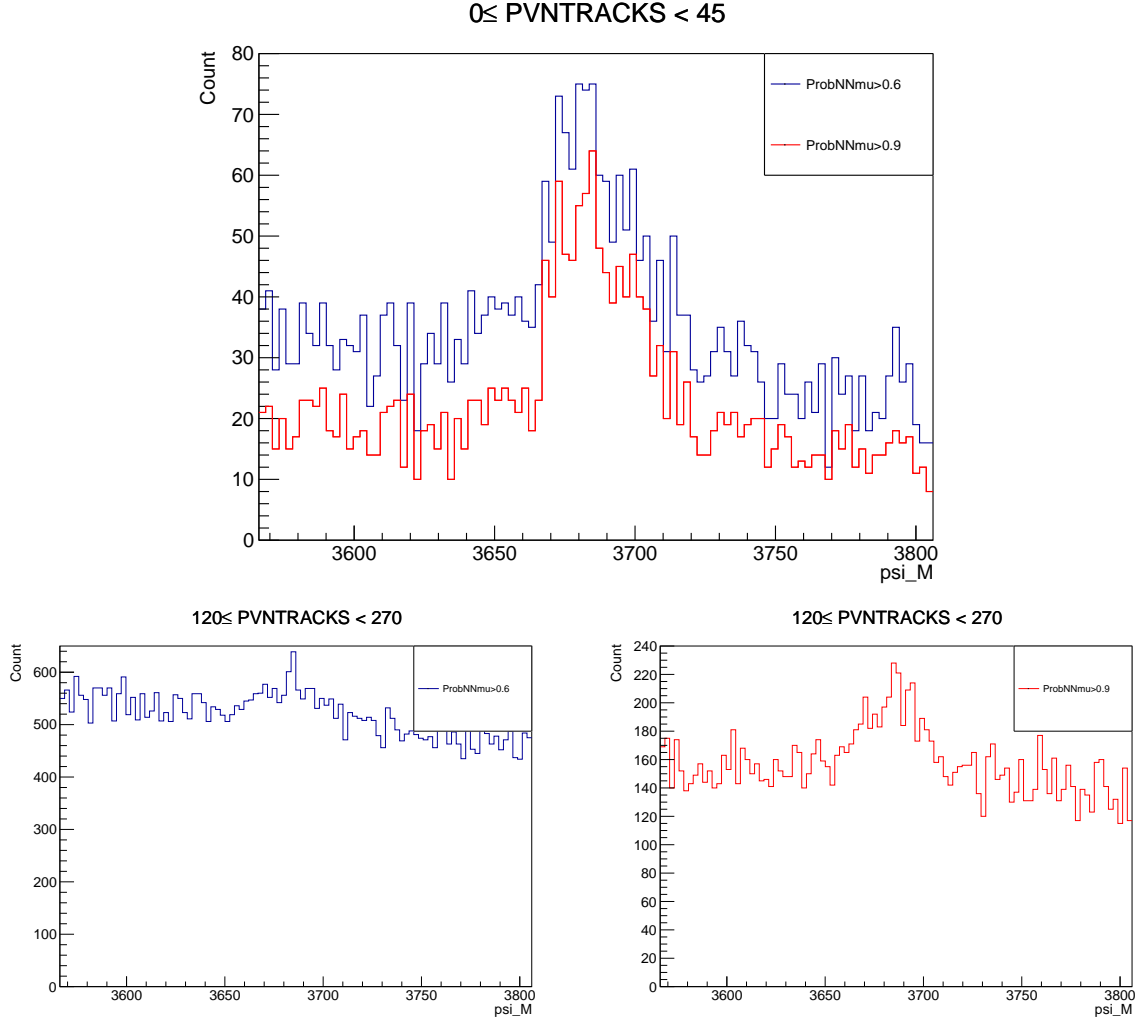
Figure 2: Mass spectrum of $\psi(2S)$ after online and offline cuts with loose PID cut (blue) and tight PID cut (red). The first row is for lowest-multiplicity class and the second row is for highest-multiplicity class.

of p_T, the transverse momentum with respect to the beam axis and of y^*, the rapidity with respect to the beam axis in the center-of-mass frame, taking the direction of the proton beam to define the polar axis, and neglecting the small angle between the two due to the crossing angle of the two beams at LHCb. The rapidity is related to the rapidity in the lab frame, y_{lab}, with $y^* = y_{lab} - 0.465$ for the pPb configuration and with $y^* = -(y_{lab} + 0.465)$ for the Pbp configuration. For pp collisions (used as reference in the various ratios given below), $y^* = y_{lab}$.

4.1 Multiplicity variables

For pPb and Pbp configurations, the variables we used to separate multiplicity classes are PVNTRACKS, nBackTracks and nForwardTracks. Cross-sections and cross-section ratios are calculated in each multiplicity class and then we can get the cross-section ratios as a function of different multiplicity variables. For the J/ψ and $\psi(2S)$ mesons, cross-sections

are extracted in the rapidity range $1.5 < y^* < 4.0 (-5.0 < y^* - 2.5)$ for pPb (Pbp), together with the transverse momentum range $0 < p_{\mathrm{T}} < 14\,\mathrm{GeV}/c$. In this analysis, we do not separate any rapidity bin or transverse momentum bin due to poor statistics of $\psi(2S)$ meson. And the systematic uncertainties due to that will be discussed throughly in chapter for systematic uncertainties. After calculating the ratio of $\psi(2S)$-to-J/ψ cross-section ratios in each multiplicity bin, we will further normalized the multiplicity variables by dividing it by the mean values from **NoBias** data samples. The binning schemes and mean values from **NoBias** data samples for different multiplicity variables are summarized in Table 8. PVNTRACKS starts at 4 since at least four tracks required to form a primary vertex.

Table 8: Binning schemes for different multiplicity variables.

Configurations	Mult. Variables	Schemes	Mean (NoBias)
pPb	PVNTRACKS	4, 45, 70, 90, 120, 270	60.54
pPb	nForwardTracks	0, 25, 43, 57, 72, 150	33.17
pPb	nBackTracks	0, 17, 29, 40, 54, 180	27.37
Pbp	PVNTRACKS	4, 60, 90, 120, 160, 330	69.54
Pbp	nForwardTracks	0, 35, 65, 85, 110, 250	47.07
Pbp	nBackTracks	0, 13, 22, 30, 47, 120	22.47

4.2   Cross-sections and cross-section ratios

The absolute double differential cross-sections for J/ψ or $\psi(2S)$ production are defined in Eq 2.

$$\frac{\mathrm{d}^2\sigma}{\mathrm{d}y^*\mathrm{d}p_{\mathrm{T}}}\bigg|_{Mult.\ bin} = \frac{N}{\mathcal{L} \times \epsilon_{\mathrm{tot}} \times \mathcal{B}_{\mu\mu} \times \Delta y^* \times \Delta p_{\mathrm{T}}}\bigg|_{Mult.\ bin}. \tag{2}$$

where N represents the raw yield of the J/ψ or $\psi(2S)$ reconstructed in the given multiplicity bin within the rapidity and transverse momentum ranges mentioned above, ϵ_{tot} the total efficiency, including acceptance, $\mathcal{B}_{\mu\mu}$ the branching ratio of the J/ψ or $\psi(2S)$ decay in two muons and $\mathcal{L}$ the integrated luminosity of the given data sample. The values of branching ratio $\mathcal{B}(J/\psi \to \mu^+\mu^-) = (5.961 \pm 0.033)\%$ is the branching fraction of the decay $J/\psi \to \mu^+\mu^-$, and $\mathcal{B}(\psi(2S) \to e^+e^-) = (7.93 \pm 0.17) \times 10^{-3}$ is the branching fraction of the decay $\psi(2S) \to e^+e^-$, quoted from the PDG 2022 review [22]. The dielectron branching fraction is used for $\psi(2S)$ since it has a much smaller uncertainty than the dimuon one. Assuming lepton universality, the later is used to compute the cross-section. Cross-section ratio is defined in Eq. 3. The width of rapidity, transverse momentum and integrated luminosity are canceled out.

$$\frac{\mathrm{d}^2\sigma_{\psi(2S)}/\mathrm{d}y^*\mathrm{d}p_{\mathrm{T}}}{\mathrm{d}^2\sigma_{J/\psi}/\mathrm{d}y^*\mathrm{d}p_{\mathrm{T}}}\bigg|_{Mult.\ bin} = \frac{\mathcal{B}(J/\psi \to \mu^+\mu^-)}{\mathcal{B}(\psi(2S) \to e^+e^-)} \times \frac{N_{\psi(2S)}}{N_{J/\psi}}\bigg|_{Mult.\ bin} \times \frac{\epsilon_{\mathrm{tot},J/\psi}}{\epsilon_{\mathrm{tot},\psi(2S)}}\bigg|_{Mult.\ bin}. \tag{3}$$

5 Signal extraction

The numbers of prompt and from-b J/ψ and $\psi(2S)$ signal candidates are extracted from a simultaneous fit to the invariant mass and pseudo-proper time t_z distributions. For prompt production, t_z is equal to 0 while for charmonium coming from the decay of a B hadron, t_z is a good approximation of the B hadron propertime and should follow an exponential distribution.

5.1 Mass fit function

The procedure that is described in the following is very close to the one used in previous pp analyses [23]. The function describing the invariant mass of the signal candidates is a Crystal Ball function defined in Eq. 4.

$$f_{\mathrm{CB}}(m; \mu, \sigma, \alpha, n) = \begin{cases} \left(\frac{n}{|\alpha|}\right)^n e^{-\frac{1}{2}\alpha^2}\left(\frac{n}{|\alpha|} - |\alpha| - \frac{m-\mu}{\sigma}\right)^{-n} & \frac{m-\mu}{\sigma} < -|\alpha| \\ \exp\left(-\frac{1}{2}\left(\frac{m-\mu}{\sigma}\right)^2\right) & \frac{m-\mu}{\sigma} > -|\alpha|. \end{cases} \quad (4)$$

The value of the parameter n is fixed to 1 following the physics arguments described in Ref. [24], while the value of the parameter α is constrained from the values of the resolution parameter σ following

$$\alpha = 2.066 + 0.0085\sigma - 0.00011\sigma^2, \quad (5)$$

extracted from toy Monte Carlo studies and where σ is expressed in MeV. The background, which is only combinatorial, is described by an exponential function,

$$f_{bkg}(x; p) = e^{-px}. \quad (6)$$

For J/ψ mass fit, two crystal ball function with common mean value are applied to describe the signals while for $\psi(2S)$, only one is used.

5.2 Pseudo-propertime fit function

To determine the signal yields of prompt and from-b components separately, the t_z distribution is used. In each kinematic and multiplicity bin, an unbinned extended maximum likelihood fit to the two-dimension distributions of invariant mass $m(\mu^+\mu^-)$ and t_z is performed to separate prompt component from that from b. At the generator level, the t_z distribution of the prompt component is a Dirac delta function, $\delta(t_z)$, while that from b follows an exponential function as seen from simulation. For J/ψ and $\psi(2S)$ signals, the detector resolution is taken into account by convolving a resolution function, which is described by the sum of two Gaussian functions with a common mean and resolution parameters σ and 2σ respectively:

$$f_{\mathrm{resolution}}(t_z; \mu, \sigma, \beta) = \frac{\beta}{\sqrt{2\pi}\sigma}e^{-\frac{(t_z-\mu)^2}{2\sigma^2}} + \frac{1-\beta}{2\sqrt{2\pi}\sigma}e^{-\frac{(t_z-\mu)^2}{8\sigma^2}}. \quad (7)$$

The background control sample consists of random combinations of muons from semi-leptonic b and c decays, which tend to produce positive t_z values, as well as mis-reconstructed tracks from decays-in-flight of kaons and pions, which contribute both

11

269 to positive and negative t_z values. The t_z distribution of the background is therefore mod-
270 eled with an empirical function, composed of a Dirac delta function and five exponentials
271 (three for positive t_z and two for negative t_z, with one positive t_z and one negative sharing
272 the same slope parameter). This function is convolved with the sum of two Gaussian
273 functions as a resolution function, which has different parameters as for signals. The fit
274 function for t_z background is as follows,

$$
f_{\text{background}} = \left[(1 - f_1 - f_2 - f_3 - f_4)\delta(t_z) + \theta(t_z)(\frac{f_1}{\tau_1}e^{-t_z/\tau_1} + \frac{f_2}{\tau_2}e^{-t_z/\tau_2}) \right.
$$
$$
\left. + \theta(-t_z)\frac{f_3}{\tau_3}e^{t_z/\tau_3} + \frac{f_4}{2\tau_4}e^{-|t_z|/\tau_4} \right] * \left(\frac{\beta'}{\sqrt{2\pi}S_1'\sigma}e^{-\frac{(t_z-\mu)^2}{2S_1'^2\sigma^2}} + \frac{1-\beta'}{\sqrt{2\pi}S_2'\sigma}e^{-\frac{(t_z-\mu)^2}{2S_2'^2\sigma^2}} \right).
$$

(8)

275 The shape of the background is chosen empirically based on the shape seen in the t_z
276 distribution of the J/ψ and $\psi(2S)$ mass side-bands, which are at 50 MeV/c^2 away from
277 the mass values from the PDG. The fit procedures are as follows,

- First step, the one-dimensional fit to the mass spectrum is performed to estimate the
278 yield and the parameters of inclusive (sum of prompt and from-b) signal candidates,
280 the background yield and of the exponent of the background function.

- Second step, the mass sideband candidates ($|M - M^{PDG}| > 50\,\text{MeV}/c^2$) are used to
282 fit the t_z distribution for the background.

- Last step, a simultaneous fit to the mass and the pseudo-proper decay time distribu-
284 tions is then performed.

285 As examples, the t_z background fit for J/ψ and $\psi(2S)$ are shown in Figure 3 for
286 $4 \leq PVNTRACKS < 45$ in pPb configurtion and the 2-dimensional fit projected in mass
287 spectrum and t_z spectrum are shown in Figure 4 for $4 \leq PVNTRACKS < 45$ in pPb
288 configuration. The fit results for other multiplicity class in pPb and Pbp configurations
289 can be found in appendix.

6 Efficiency determination

291 The number of signal candidates are corrected by the total efficiency to obtain the $\psi(2S)$-
292 to-J/ψ cross-section ratio measurements. The efficiencies are assumed to be equal for
293 prompt and from-b signals as can be seen for example in the measurement of J/ψ cross-
294 section at 13 TeV. The total efficiency is the product of the acceptance efficiency (ϵ_{acc}),
295 the reconstruction and selection efficiency ($\epsilon_{\text{Reco\&Sel}}$), the particle identification efficiency
296 (ϵ_{MuonID}), the trigger efficiency ($\epsilon_{\text{Trigger}}$). The acceptance efficiency is calculated for all
297 multiplicity classes. The others are calculated in each multiplicity class. And according
298 to Eq. 3, we are going to find the efficiency ratio in each multiplicity class. The ratio of
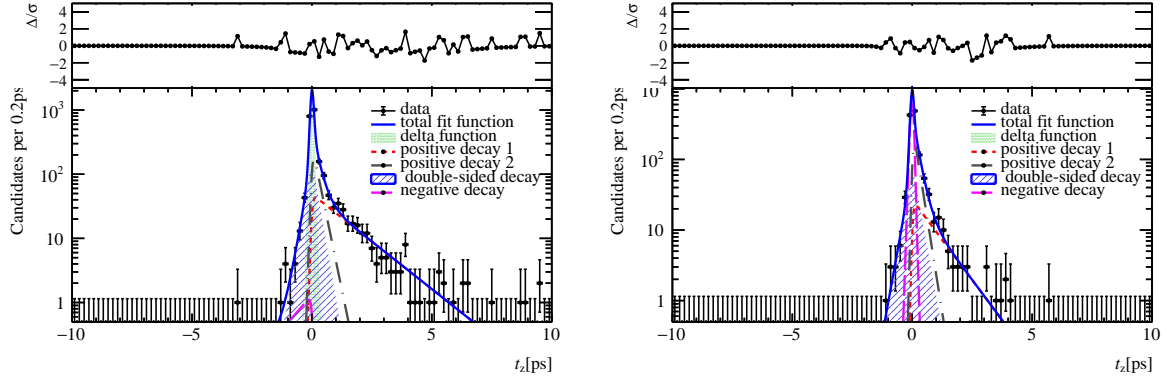
12

Figure 3: t_z background fit for J/ψ (left) and $\psi(2S)$ (right) for $4 \leq PVNTRACKS < 45$ in pPb configuration.
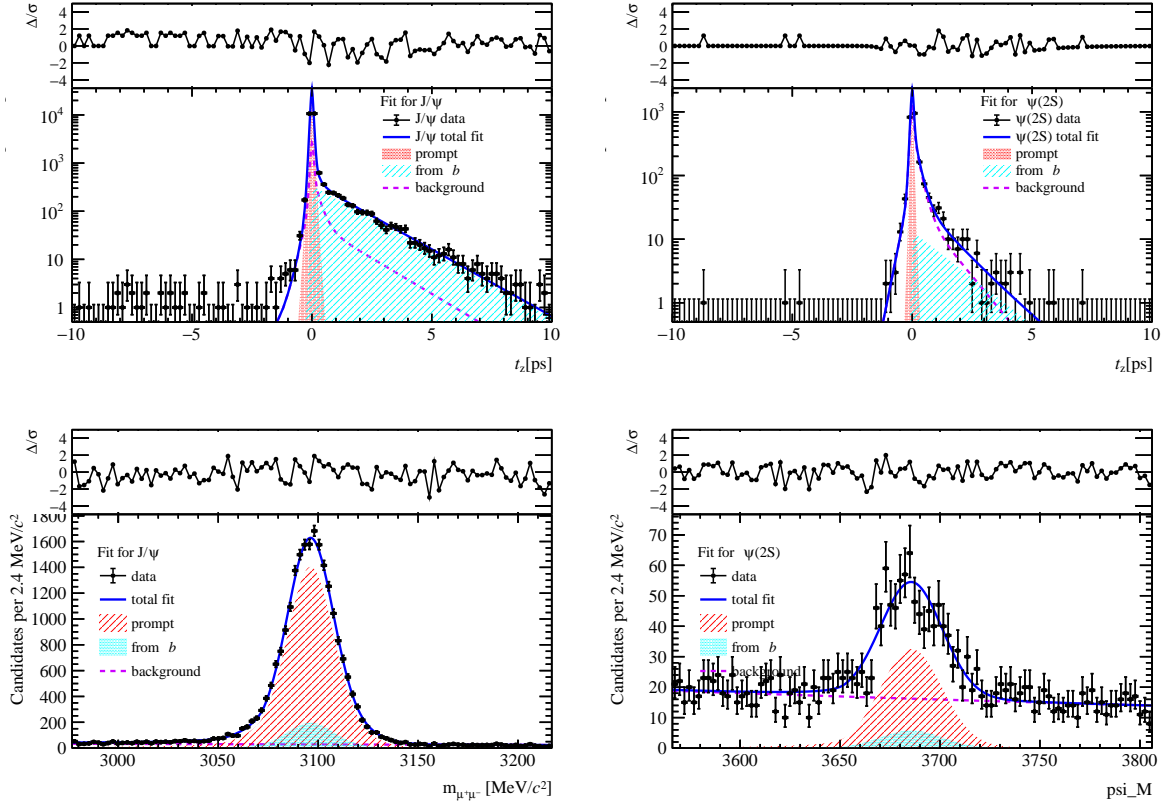

Figure 4: 2-Dimensional fit projected on t_z spectrum (first row) and mass spectrum (second row) for J/ψ (left) and $\psi(2S)$ (right) for $4 \leq PVNTRACKS < 45$ in pPb configuration.

13

total efficiencies for J/ψ and $\psi(2S)$ is defined in the following equation 9.

$$
\begin{aligned}
R_{tot} &= \frac{\epsilon_{\text{tot},J/\psi}}{\epsilon_{\text{tot},\psi(2S)}}\bigg|_{Mult.\ bin} \\
&= \frac{\epsilon_{\text{acc},J/\psi}}{\epsilon_{\text{acc},\psi(2S)}} \times \frac{\epsilon_{\text{Reco\&Sel},J/\psi} \cdot \epsilon_{\text{MuonID},J/\psi} \cdot \epsilon_{\text{Trigger},J/\psi}}{\epsilon_{\text{Reco\&Sel},\psi(2S)} \cdot \epsilon_{\text{MuonID},\psi(2S)} \cdot \epsilon_{\text{Trigger},\psi(2S)}}\bigg|_{Mult.\ bin} \\
&= R_{acc} \times R_{eff}|_{Mult.\ bin},
\end{aligned}
\tag{9}
$$

where R_{acc} is the ratio of acceptance efficiencies of J/ψ to $\psi(2S)$ and R_{eff} is the ratio of the rest efficiencies of J/ψ and $\psi(2S)$. All steps are determined from simulation, with truth matched signal decays, except for the tracking efficiency and the particle identification, where data driven methods are used to correct the efficiencies obtained from the simulation. Their exact definitions are given in the following subsections. In the simulation, J/ψ and $\psi(2S)$ mesons are assumed produced without polarization. For the simulation samples used for this analysis, the truth matching efficiency is equal to $99.5 \pm 0.1\%$ for both pPb and Pbp samples. It is assumed to be independent of p_{T} and y^*.

6.1   Re-weight on Monte Carlo sample

The distribution of PVNTRACKS, nForwardTracks and nBackTracks of Monte Carlo and s-weight data for both J/ψ and $\psi(2S)$ in pPb and Pbp configurations are compared. As an example, we draw the distributions for Monte Carlo and s-weight data in pPb configuration in Figure 5. We can see that the multiplicity distribution for J/ψ and $\psi(2S)$ signals both in Monte Carlo sample and s-weight data are compatible within uncertainties. And what we want in the end is the ratio of total efficiencies. The bias caused by the difference in multiplicity should be canceled.
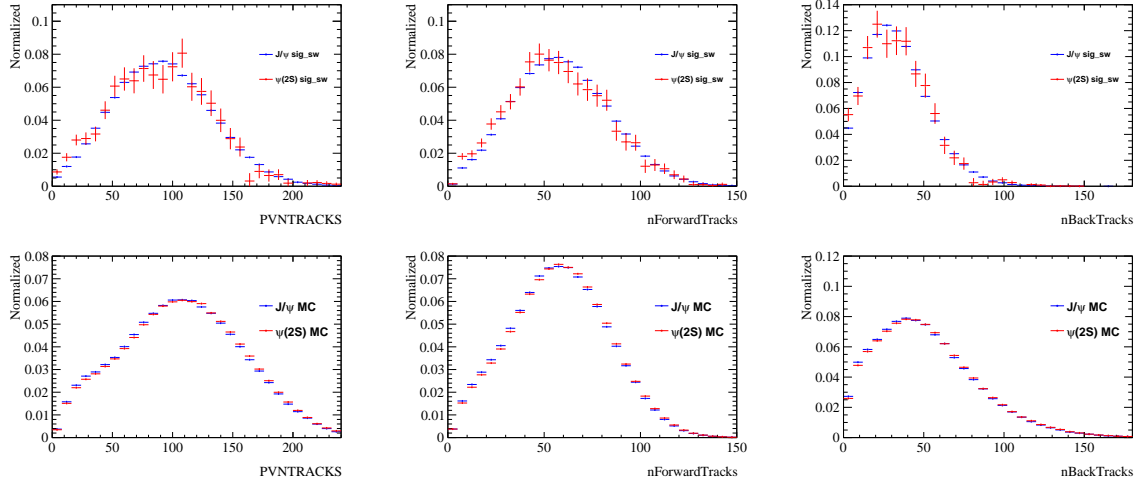

Figure 5: Distribution of multiplicity variables for s-weight data (first row) and MC (second row) in pPb configuration.

The difference in Monte Carlo sample and s-weight data for J/ψ and $\psi(2S)$ should cancel. But the distribution of transverse momentum and rapidity in high- and low-

14

multiplicity for both J/ψ and $\psi(2S)$ is not negligible. So two samples of high- and low-multiplicity classes are considered when re-weighting Monte Carlo sample to match s-weight data (the high- and low-multiplicity samples are seperated by the mean values of multiplicity variables we choose accordingly). As an example, the re-weight of p_T and y^* for high- and low-multiplicity J/ψ samples when taking PVNTRACKS as multiplicity variable is shown in Figure 6. And that for $\psi(2S)$ is shown in Figure 7.
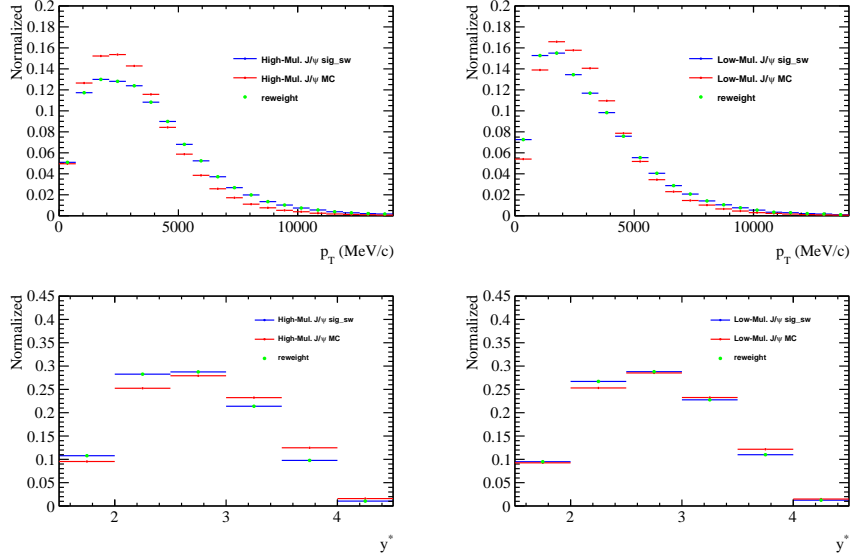
Figure 6: Re-weight of p_T (first row) and y^* (second row) for high- (left) and low-multiplicity (right) J/ψ samples in pPb configuration.
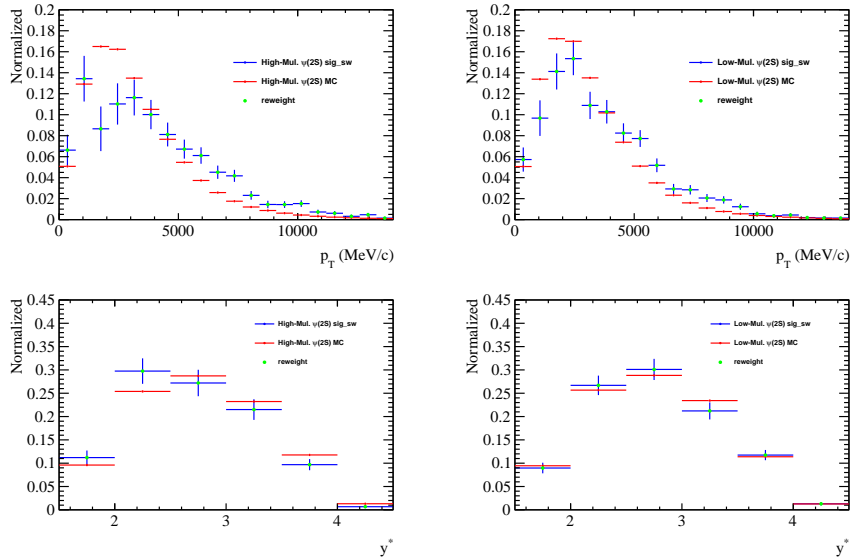
Figure 7: Re-weight of p_T (first row) and y^* (second row) for high- (left) and low-multiplicity (right) $\psi(2S)$ samples in pPb configuration.

15

6.2 Acceptance

The acceptance efficiency is defined as

$$\epsilon_{\text{acc}}(p_{\text{T}}, y^*) = \frac{J/\psi(\psi(2S)) \text{ in bin } (p_{\text{T}}, y^*) \text{ with both } \mu \text{ in LHCb}}{J/\psi(\psi(2S)) \text{ generated in bin } (p_{\text{T}}, y^*)} \tag{10}$$

It is estimated from generator-level only simulations, using the settings described in Sect 2. Both μ in LHCb means here that they have a pseudo-rapidity η between 2 and 5, before the magnet. In this analysis we only care about the ratio of acceptance efficiencies R_{acc}. When calculating the ratio of acceptance efficiencies, 50 random re-weight tables of p_{T} and y^* from high- and low-multiplicity samples are generated (100 in total) for both J/ψ and $\psi(2S)$, within each bin a Gaussian random number is generated with mean the content and sigma the uncertainty. Then the 100 tables are introduced as correction to acceptance efficiencies. Then 100 ratios of acceptance efficiencies are calculated. Fit 100 R_{acc} values with a Gaussian function we get the mean value as the ratio of acceptance efficiencies and the sigma be its systematic uncertainty. As an example, the fit result for R_{acc} when global cuts for PVNTRACKS as multiplicity are applied is shown in Figure 8. The value is as follows,

$$R_{acc} = \frac{\epsilon_{\text{acc},J/\psi}}{\epsilon_{\text{acc},\psi(2S)}} = 0.991 \pm 0.012. \tag{11}$$
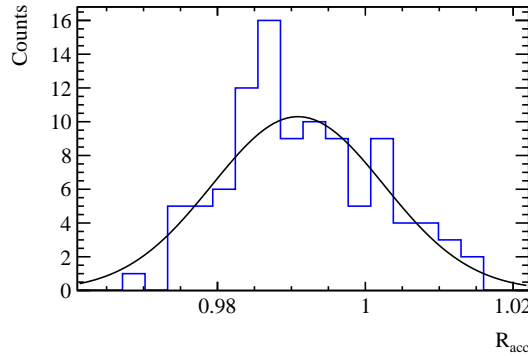

Figure 8: Fit Gaussian function on the distribution of R_{acc} from 100 trials with global cuts for PVNTRACKS as multiplicity variable.

6.3 Reconstruction and selection efficiency

The reconstruction and selection efficiency is defined as the fraction of J/ψ ($\psi(2S)$) in the acceptance, where both muons are reconstructed as long tracks and then pass the offline selections,

$$\epsilon_{\text{Reco\&Sel}}(p_{\text{T}}, y^*) = \frac{J/\psi(\psi(2S)) \text{ in bin } (p_{\text{T}}, y^*) \text{ with both } \mu \text{ reconstructed and selected}}{J/\psi(\psi(2S)) \text{ in bin } (p_{\text{T}}, y^*) \text{ with both } \mu \text{ in LHCb}}. \tag{12}$$

Then the reconstruction efficiency is further corrected using the data-over-simulation single tracking efficiency ratio. The ratio of tracking efficiencies for a single track in data
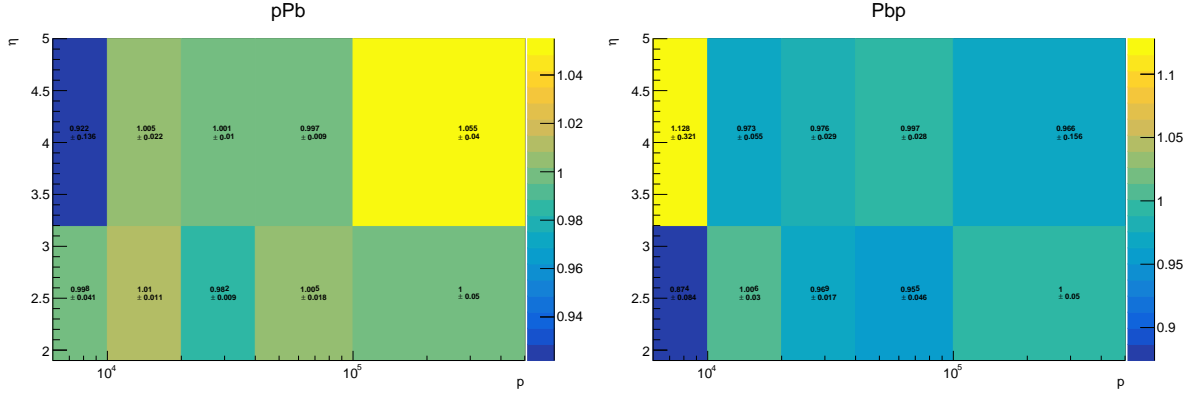
16

Figure 9: Ratio between data and pPb (left) and Pbp simulation of per-track tracking efficiency in bins of the track η and p.

and simulation determined with the Long Tag-Probe method is shown in Figure 9 which was given by the tracking group. For a given event the correction factor is determined by multiplying the efficiency ratios for each of the tracks in the final state.

From Eq. 9 we can see that, we calculate the ratio of all the efficiencies R_{eff} (except for acceptance efficiencies) as a whole part, since they are all calculated with full-simulation Monte Carlo sample. Another reason is, when calculating $\epsilon_{\text{Reco\&Sel}}$, ϵ_{MuonID} and $\epsilon_{\text{Trigger}}$, 500 random tables of p_{T} and y^* from high- and low-multiplicity samples are generated (1000 in total) for both J/ψ and $\psi(2S)$ in pPb and Pbp configurations and introduced to correct the imperfection on simulation to data. For a certain trial, the re-weight on p_{T} (or y^*) may under- or over-estimate $\epsilon_{\text{Reco\&Sel}}$, ϵ_{MuonID} and $\epsilon_{\text{Trigger}}$ simultaneously, it is hard to determine the dependence between these efficiencies. So a good way is to calculate them as a whole, each time a certain random re-weight table is introduced. The definition of R_{eff} is in Eq. 13.

$$
R_{eff}\bigg|_{Mult.\ bin} = \frac{\epsilon_{\text{Reco\&Sel},J/\psi} \cdot \epsilon_{\text{MuonID},J/\psi} \cdot \epsilon_{\text{Trigger},J/\psi}}{\epsilon_{\text{Reco\&Sel},\psi(2S)} \cdot \epsilon_{\text{MuonID},\psi(2S)} \cdot \epsilon_{\text{Trigger},\psi(2S)}}\bigg|_{Mult.\ bin}. \tag{13}
$$

Similarly, 1000 random tables for data-over-simulation single tracking efficiency ratio are generated and introduced into the 1000 trials, and 1000 random tables for efficiency table obtained from PIDCalib package are introduced in each trial as well to calculate PID efficiencies, and hence, R_{eff}, as stated in the following part. So we will give an overall estimation (values and uncertainties) for R_{eff} after introduced ϵ_{MuonID} and $\epsilon_{\text{Trigger}}$.

6.4   PID efficiency

The PID efficiency is defined as

$$
\epsilon_{\text{MuonID}}(p_{\text{T}}, y^*) = \frac{J/\psi(\psi(2S)) \text{ satisfying PID selection in bin } (p_{\text{T}}, y^*)}{J/\psi(\psi(2S)) \textbf{ selected in bin } (p_{\text{T}}, y^*)}. \tag{14}
$$

The PID efficiency for muons is taken from data using calibration tables (PIDCalib tables) obtained from control samples, namely J/ψ candidates. These calibration tables give the efficiency of the PID selections as a function of the pseudo-rapidity, of the total momentum

of the muon tracks and of the track multiplicity of the event estimated from the number of hits in the SPD. They are available for the pp, pPb and Pbp data taking. The muon ID efficiency in each (p_T, y^*) bin is then calculated by averaging the muon ID efficiency of each candidate in the bin, which is the product of the muon ID efficiencies of the two muons from the efficiency table, according to their $(p, \eta, nSPDhits)$ values. As mentioned above, calculation on ϵ_{MuonID} for J/ψ and $\psi(2S)$ is only a section of calculation of R_{eff}. So 1000 random tables are generated from the PIDCalib efficiency table and introduced to each trial of R_{eff} calculations.

6.5 Trigger efficiency

The trigger efficiency is defined as follows

$$\epsilon_{\text{Trigger}}(p_T, y^*) = \frac{J/\psi(\psi(2S)) \text{ TOS of L0 and HLT1 in bin } (p_T, y^*)}{J/\psi(\psi(2S)) \textbf{ selected in bin } (p_T, y^*)}, \qquad (15)$$

where the selection includes here the PID requirements. The efficiencies are computed with the simulated samples, applying on them the simulation of the PID. Note that since the analysis is done on the TURBO candidates, the efficiency of the HLT2 is included in the reconstruction, PID and selection efficiencies. When calculating the trigger efficiencies for J/ψ and $\psi(2S)$, same random tables generated from re-weight tables of p_T and y^* are used as that used in $\epsilon_{\text{Reco\&Sel}}$ and ϵ_{MuonID} above for each one of the 1000 trials.

6.6 Total efficiency

Finally, the 1000 ratios of all the efficiencies except geometric acceptance R_{eff}'s are fitted with a Gaussian function. Hence, we can calculate the ratio of total efficiencies $R_{tot} = R_{acc} \times R_{eff}$ with systematic uncertainties arised from,

- re-weight of p_T distribution from high- and low-multiplicity samples,

- re-weight of y^* distribution from high- and low-multiplicity samples,

- uncertainties due to the limit calibration sample size in PIDCalib efficiency table,

- uncertainties of data-over-simulation ratio of per tracking efficiency.

Systematic uncertainties from other sources will be discussed in Sec 7. As an example, the fit results for R_{eff} in different PVNTRACKS classes for pPb configuration are shown in Figure 10. The corresponding values of R_{eff} with uncertainties mentioned above are summarized in Table 9. Fit plots and summary tables for other multiplicity variables and configurations can be found in appendix.
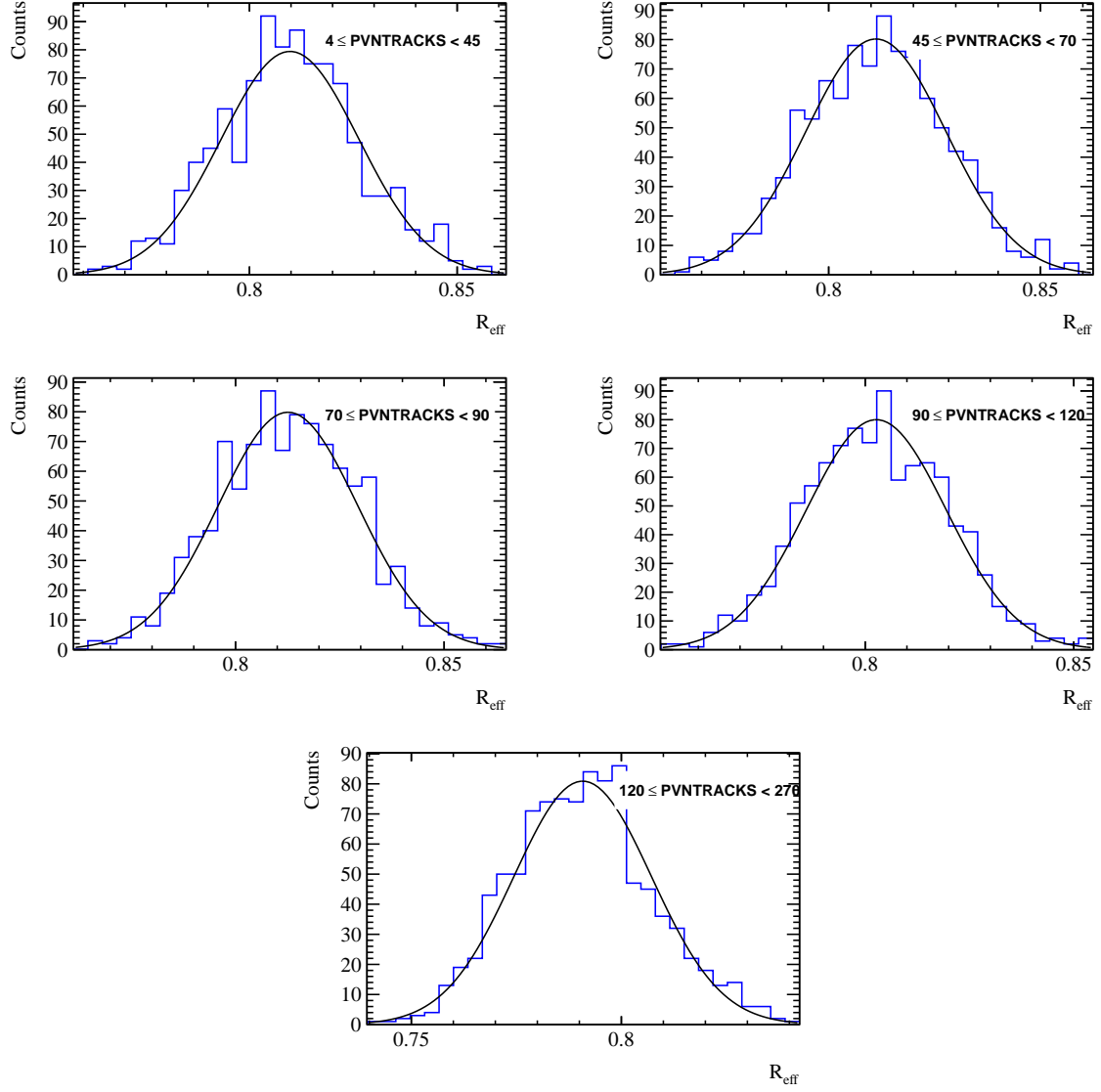
Figure 10: Fit Gaussian functions on the distributions of 1000-trial R_{eff}'s in different PVN-TRACKS classes.

Table 9: R_{eff} in different PVNTRACKS regions in pPb configuration.

$4 \leq$ PVNTRACKS < 45	0.810 ± 0.021
$45 \leq$ PVNTRACKS < 70	0.811 ± 0.020
$70 \leq$ PVNTRACKS < 90	0.813 ± 0.021
$90 \leq$ PVNTRACKS < 120	0.803 ± 0.021
$120 \leq$ PVNTRACKS < 270	0.791 ± 0.021

7   Other Systematic uncertainties

Before we proceed this section, we state some systematic uncertainties mentioned in previous sections, and add some conclusions on those which are simple to handle as follow,

- re-weight of p_T distribution from high- and low-multiplicity samples (for ratios of ϵ_{acc} and the other efficiencies),

- re-weight of y^* distribution from high- and low-multiplicity samples (for ratios of ϵ_{acc} and the other efficiencies),

- uncertainties due to the limit calibration sample size in PIDCalib efficiency table (for ratios of efficiencies except ϵ_{acc}),

- uncertainties of data-over-simulation ratio of per tracking efficiency(for ratios of efficiencies except ϵ_{acc}),

- global cut of nVeloClusters < 8000 (negligible),

- uncertainty of luminosity is canceled when calculating the ratio of $\psi(2S)$-to-J/ψ production,

- relative uncertainty due to branching fraction is calculated to be 2.2%, this term is not considered when calculating the normalized ratio as function of multiplicity, but when we compare ratio in forward and backward regions, we do not normalize the ratio, hence, need to consider it in this case.

Other systematic uncertainties are reported in this section.

7.1   Monte Carlo statistics

This uncertainty is the statistical error on the ratio of efficiencies in different multiplicity bins, due to the finite size of the simulation samples. The uncertainty varies from 0.02% to 0.2% over all multiplicity classes divided by three multiplicity variables and in pPb and Pbp configurations, which is negligible compared to other systematic uncertainties.

7.2   Signal extraction

The choice of the fit model for the mass and t_z distributions affects the number of events. In Sec 5 we have mentioned that two CB functions with common mean are used for J/ψ mass fitwhile only one is used for $\psi(2S)$. The uncertainty associated with the choice of the signal mass function is estimated using a different function of two CB functions for $\psi(2S)$. Two CB functions have common mean, the α values for both CB functions are determined by the Eq. 5. And the width of wider CB function is determined by $\sigma_2 = sigma_1 + 25.7$, the ratio of the narrower one is fixed to 0.96 according to the study in 13.TeV pp collisions [25]. New fit model for $\psi(2S)$ mass spectrum is introduced and then a new two-dimensional fit for mass and t_z is performed. Then the difference in ratio of $\psi(2S)$-to-J/ψ ratio and the statistical uncertainty of the ratio in each PVNTRACKS bin are shown in Figure 11.
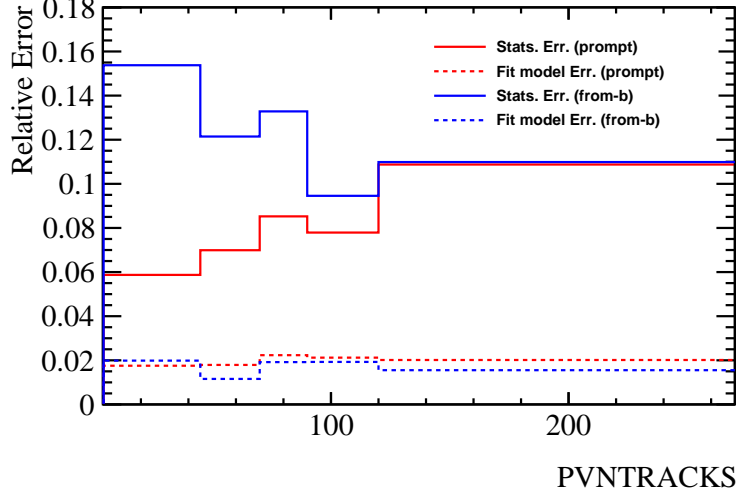
Figure 11: The statistical uncertainties and the systematic uncertainty arised from different fit model of $\psi(2S)$-to-J/ψ ratio.

We can see that the variation caused by different fit model is totally merged by the statistical uncertainties, the statistical uncertainty is larger than the uncertainty caused by fit model by at least a factor of 3. Which means we can completely treat the difference caused by fit model as statistical fluctuation, hence, negligible.

7.3 Trigger efficiency

The trigger efficiency in simulation is cross-checked with data, and the resulting difference in the ratio of $\epsilon_{\text{Trigger}}$ between simulation and data is quoted as a systematic uncertainty. If the statistical uncertainties of the ratio arised from fitting the TIS and TISTOS sample of J/ψ and $\psi(2S)$ are larger, then it will be quoted as systematic uncertainty. For both L0Muon and Hlt1DiMuonHighMass the TISTOS method is used to evaluate the efficiency for L0Muon && Hlt1DiMuonHighMass both in simulation and data. We use L0Global as the TIS line. As the data sample size is limited by the number of the TIS events of $\psi(2S)$ sample, the TISTOS efficiencies derived by data and Monte Carlo sample over all multiplicity and kinematic region. Due to the different global cuts under different multiplicity schemes and configurations, TISTOS method is carried out in each case and the result is summarized in Table 10.

21

Table 10: Systematic uncertainty of $\epsilon_{\text{Trigger}}$ by TISTOS method.

Configuration	Mult. Variable	Variation	Stats. Err.	Syst. Err. quoted
pPb	PVNTRACKS	2.7%	3.9%	3.9%
pPb	nForwardTracks	3.2%	3.0%	3.2%
pPb	nBackTracks	2.7%	3.9%	3.9%
Pbp	PVNTRACKS	2.0%	3.8%	3.8%
Pbp	nForwardTracks	1.7%	3.6%	3.6%
Pbp	nBackTracks	2.7%	4.1%	4.1%

7.4 Binning scheme of PID table

Uncertainty due to binning scheme of the calibration sample, studied by varying the binning method in p_μ, η_μ, and nSPDHits respectively. The default one and the two alternative binning schemes could be found below. The nominal binning scheme of the muon ID efficiency for muons we use to calculate the muon ID efficiency of J/ψ and $\psi(2S)$ mesons is defined:

- p_μ boundaries [GeV/c]: 3, 10, 20, 25, 30, 35, 40, 45, 50, 60, 70, 80, 100, 1000.

- η boundaries: 2.0, 2.5, 3.0, 3.5, 4.0, 4.5, 5.0.

- nSPDhits boundaries: 0, 300, 500, 700, 1400.

One of the two alternative binning schemes is defined:

- p_μ boundaries [GeV/c]: 3, 12.5, 22.5, 27.5, 32.5, 37.5, 42.5, 47.5, 55, 65, 75, 85, 100, 1000.

- η boundaries: 2.0, 2.6, 2.9, 3.6, 3.9, 4.5, 5.0.

- nSPDhits boundaries: 0, 250, 450, 650, 1400.

The other one binning schemes is defined:

- p_μ boundaries [GeV/c]: 3, 9, 19, 24, 29, 34, 39, 44, 49, 59, 69, 79, 100, 1000.

- η boundaries: 2.0, 2.4, 3.1, 3.4, 3.9, 4.5, 5.0.

- nSPDhits boundaries: 0, 320, 480, 720, 1400.

The maximum difference between the two new ratios calculated and the nominal ratio is quoted as the systematic uncertainty. The uncertainties are from 0.1% to 1.8%.

22

7.5   Summary of systematic uncertainties

All the systematic uncertainties are summarized in Table 11.

Table 11: Summary of systematic uncertainties on $\psi(2S)$-to-J/ψ cross-section ratio.

source	pPb	Pbp
L0&HLT	3.2%-3.9%	3.6%-4.1%
Tracking Table Uncertainty& PID Table Uncertainty& p_{T} spectrum& y spectrum	1.7%-3.6%	2.1%-3.6%
PID Table scheme	0.4%-1.7%	0.1%-1.8%
Imperfectly simulating acceptance	0.8%-1.2%	0.9%-1.3%
$\frac{\mathcal{B}(J/\psi\to\mu^+\mu^-)}{\mathcal{B}(\psi(2S)\to\mu^+\mu^-)}$ (canceled if normalized)	2.2%	2.2%
Fit model	negligible	negligible
MC sample size	negligible	negligible
Multiplicity global cut	negligible	negligible

8   Results

8.1 $\psi(2S)$-to-J/ψ ratio as function of multiplicity

With the signal yields determined from the fitting to dimuon invariant mass distributions,
the efficiency ratios estimated from simulation and calibrated control samples, and the
systematic uncertainties, the ratio of $\psi(2S)$ and J/ψ production cross-sections are measured
as a function of different multiplicity variables. As mentioned in Sec 6, the multiplicity
distribution of J/ψ and $\psi(2S)$ can be treated as the same, and due to the large uncertainty
of $\psi(2S)$ multiplicity distribution, the x-coordinate representing the multiplicity is directly
the mean value of J/ψ multiplicity distribution in each bin, normalized by the mean
value of multiplicity of NoBias data. The box represents systematic uncertainty and the
error bar represents the statistical uncertainty. In this analysis statistical uncertainty
dominates. The normalized $\psi(2S)$-to-J/ψ ratio as function of PVNTRACKS in pPb and
Pbp collisions is shown in Figure 12.

23
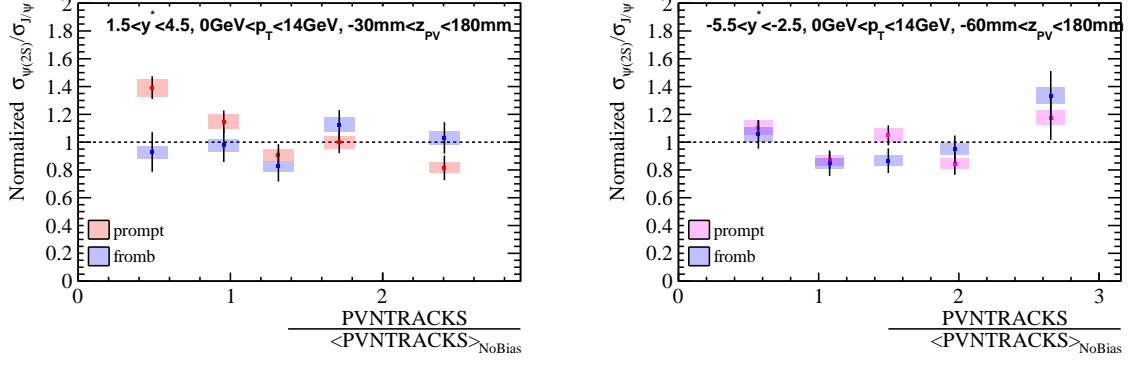
Figure 12: Normalized $\psi(2S)$-to-J/ψ ratio as function of normalized PVNTRACKS in pPb (left) Pbp (right).

We can conclude that in pPb collisions the prompt ratio decrease with increasing PVNTRACKS, while in Pbp collisions, we can not conlude any significant trend with PVNTRACKS. For J/ψ and $\psi(2S)$ from b we do not find any dependence between the ratio and multiplicity. If we compare the prompt ratio (not normalized), we should include the uncertainties branching fraction and the comparison is in Figure 13.
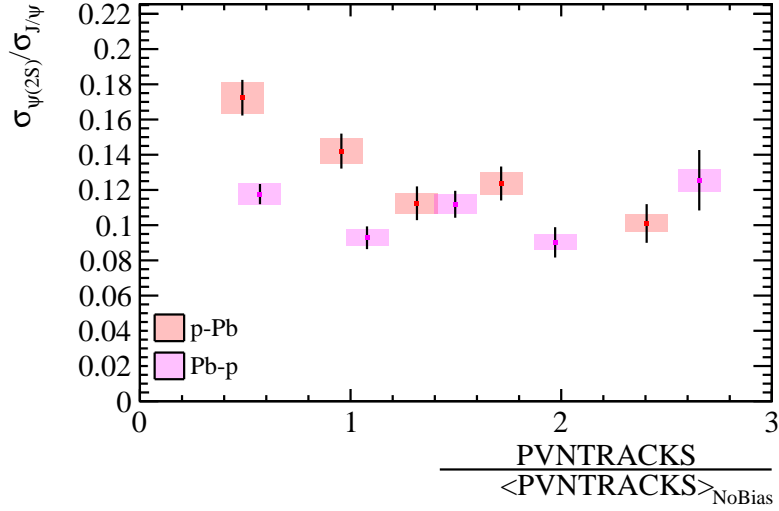
Figure 13: $\psi(2S)$-to-J/ψ ratio as function of normalized PVNTRACK.

We find the ratio in Pbp is generally lower than that in pPb collisions. This could results from the higher charged particle multiplicity in Pbp collisions, where $\psi(2S)$, with lower bounding energy, is easier to dissociate when interacting with higher amount of co-moving particles. But if this is valid, we should also observe a decreasing trend of the ratio with increasing multiplicity, which is indeed not. We furtherly measure the normalized ratio and ratio as functions of nForwardTracks, as shown in Figure 14. It comes to an agreement with the results when measuring by PVNTRACKS. The ratio of non-prompt signals is roughly constant with multiplicity in pPb and Pbp collisions. And

24

ratio of prompt signals decreases with increasing nForwardTracks in pPb, but not in Pbp collisions. If we compare the ratio in pPb and Pbp collisions, the ratios in Pbp collisions are generally lower than that in pPb collisions. But still, we do not observe a decreasing trend like in pPb collisions. Some extra mechanisms might be needed to explain the phenomenon. Since for both PVNTRACKS and nForwardTracks as multiplicity variables, we get the similar outcomes.
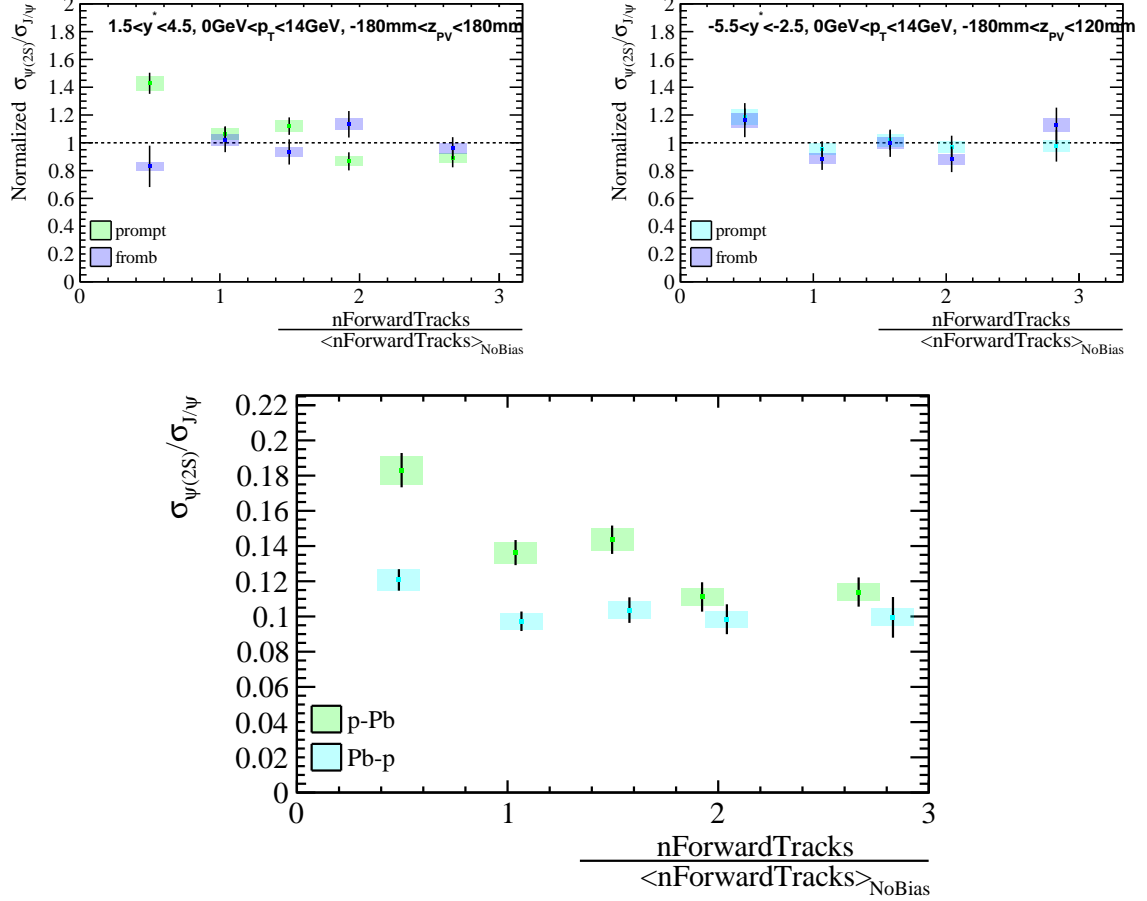

Figure 14: Normalized $\psi(2S)$-to-J/ψ ratio as function of normalized nForwardTracks in pPb (left) Pbp (right).

When multiplicity is measured by nBackTracks, as shown in Figure 15, for ratio of prompt signals, the decreasing trend is much slower with increasing nBackTracks in pPb collisions, and for Pbp, the ratio for both prompt and non-prompt signals are roughly constant. Since nBackTracks are measured in backward direction, the rapidity range is non-overlapping with where we measure the charmonia production, and co-mover effect is thought to not exist. Additionally, if QGP is not produced, the ratio should keep constant with nBackTracks. The subtle decreasing trend for ratio of prompt signals could result from the correlation between nBackTracks in pPb collisions. Similarly, there is an overall reduction on the ratio in Pbp collisions since the mean value of charged particle multiplicity is higher, which results in an overall larger amount of co-moving particles. But still, in Pbp collisions, no dependence was found between ratio and nBackTracks.

25

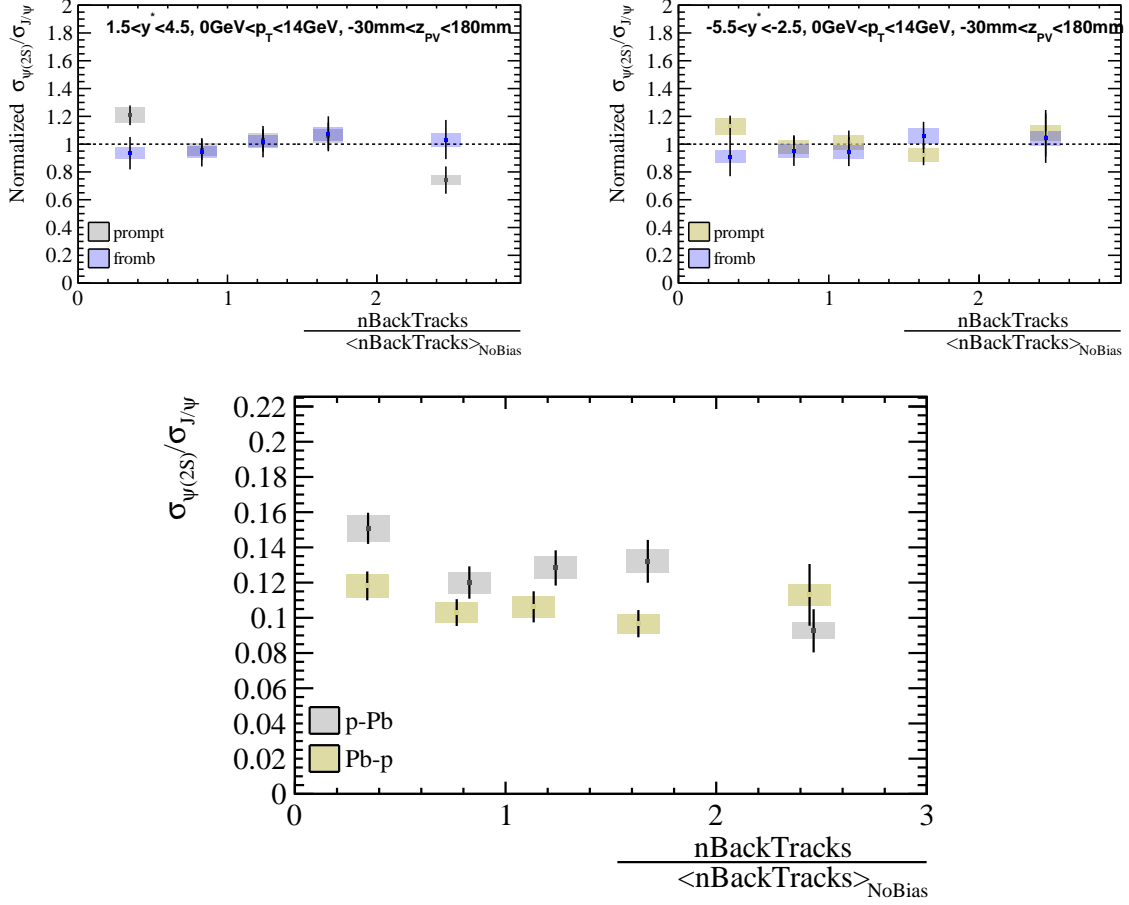Figure 15: Normalized $\psi(2S)$-to-J/ψ ratio as function of normalized nForwardTracks in pPb (left) Pbp (right).

8.2 Comparisons with other measurements

Measurements of $\mathcal{B}_{\psi(2S)}/\sigma_{\psi(2S)}$ over $\mathcal{B}_{J/\psi}/\sigma_{J/\psi}$ have been done in different collision systems at different center-of-mass energies. Results show that the value of the ratio is roughly independent of the collision systems and energies. We multiply the ratio of $\sigma_{\psi(2S)}/\sigma_{J/\psi}$ by the ratio of their branching fractions and add our measurements to the plot as follows, we find our measurements having a good agreement with others in Figs 16.
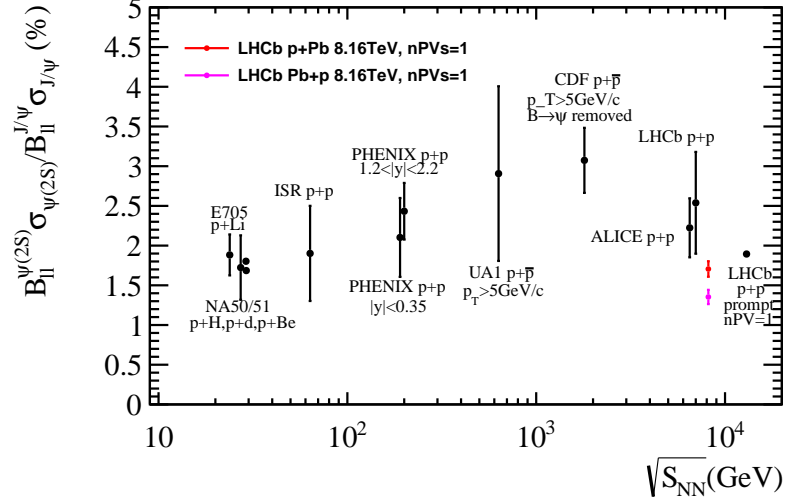
Figure 16: Comparisons of world data on the ratio of $\psi(2S)/J/\psi$ measons in dilepton decays [26–34].

9   Conclusion

The ratio of production cross-sections of $\psi(2S)$ to J/ψ in pPb and Pbp collisions at a center-of-mass energy $\sqrt{s_{NN}} = 8.16\,\mathrm{TeV}$ are reported with a data sample corresponding to an integrated luminosity of $13.6 \pm 0.3\mathrm{nb}^{-1}$ for pPb and $20.8 \pm 0.5\mathrm{nb}^{-1}$ for Pbp collected by the LHCb detector in 2016. The (normalized) ratios of prompt and non-prompt $\psi(2S)$-to-J/ψ production, as functions of different multiplicity variables, are measured in region of $0\,\mathrm{GeV} < p_\mathrm{T} < 14\,\mathrm{GeV}$ and $1.5 < y^* < 4.5$ for pPb and $-5.5 < y^* < -2.5$ for Pbp. In pPb collisions, we see an obvious decreasing trend for ratio of prompt production as a function of PVNTRACKS and nForwardTracks in pPb and a slower decrease as a function of nBackTracks. In Pbp collisions, even though the ratios have an overall lower value compared to pPb with same multiplicity scheme, the prompt and non-prompt $\psi(2S)$-to-J/ψ ratio does not show an obvious decrease as in pPb. The overall ratios in pPb and Pbp show good agreements with other measurements in different collision systems at different energies.

27

A. Table of ratios

In the appendix, we attach the ratios only, one can easily get the normalized ratios by simple calculations. Remember to cut off 2.2% relative systematic uncertainties from uncertainties of branching ratios.

Table 12: Ratio(%) of production cross-section for $\psi(2S)$ to J/ψ. The first uncertainties are statistical, the second are the systematic uncertainties.

pPb					
PVNTRACKS	4 45	45 70	70 90	90 120	120 270
prompt	$0.172 \pm 0.010 \pm 0.009$	$0.142 \pm 0.010 \pm 0.007$	$0.112 \pm 0.010 \pm 0.006$	$0.124 \pm 0.010 \pm 0.006$	$0.101 \pm 0.011 \pm 0.005$
from-b	$0.219 \pm 0.034 \pm 0.013$	$0.230 \pm 0.028 \pm 0.012$	$0.195 \pm 0.026 \pm 0.010$	$0.265 \pm 0.025 \pm 0.013$	$0.243 \pm 0.027 \pm 0.011$
Pbp					
PVNTRACKS	4 60	60 90	90 120	120 160	160 330
prompt	$0.118 \pm 0.006 \pm 0.006$	$0.093 \pm 0.006 \pm 0.005$	$0.112 \pm 0.008 \pm 0.006$	$0.090 \pm 0.009 \pm 0.005$	$0.126 \pm 0.017 \pm 0.006$
from-b	$0.240 \pm 0.023 \pm 0.013$	$0.193 \pm 0.021 \pm 0.010$	$0.197 \pm 0.020 \pm 0.011$	$0.216 \pm 0.022 \pm 0.010$	$0.304 \pm 0.040 \pm 0.015$

Table 13: Ratio(%) of production cross-section for $\psi(2S)$ to J/ψ. The first uncertainties are statistical, the second are the systematic uncertainties.

pPb					
ForTRACKS	0 25	25 43	43 57	57 72	72 150
prompt	$0.183 \pm 0.010 \pm 0.008$	$0.136 \pm 0.007 \pm 0.006$	$0.144 \pm 0.008 \pm 0.006$	$0.111 \pm 0.008 \pm 0.005$	$0.114 \pm 0.008 \pm 0.005$
from-b	$0.192 \pm 0.034 \pm 0.010$	$0.236 \pm 0.021 \pm 0.011$	$0.216 \pm 0.021 \pm 0.010$	$0.262 \pm 0.022 \pm 0.010$	$0.222 \pm 0.018 \pm 0.009$
Pbp					
ForTRACKS	0 35	35 65	65 85	85 110	110 250
prompt	$0.121 \pm 0.006 \pm 0.006$	$0.097 \pm 0.006 \pm 0.005$	$0.104 \pm 0.007 \pm 0.005$	$0.098 \pm 0.008 \pm 0.005$	$0.099 \pm 0.012 \pm 0.005$
from-b	$0.262 \pm 0.028 \pm 0.014$	$0.199 \pm 0.018 \pm 0.010$	$0.225 \pm 0.022 \pm 0.011$	$0.198 \pm 0.021 \pm 0.010$	$0.255 \pm 0.027 \pm 0.012$

Table 14: Ratio(%) of production cross-section for $\psi(2S)$ to J/ψ. The first uncertainties are statistical, the second are the systematic uncertainties.

| pPb					
BackTRACKS	0 17	17 29	29 40	40 54	54 180
prompt	$0.151 \pm 0.009 \pm 0.008$	$0.120 \pm 0.009 \pm 0.006$	$0.128 \pm 0.010 \pm 0.007$	$0.132 \pm 0.012 \pm 0.007$	$0.093 \pm 0.012 \pm 0.005$
from-b	$0.219 \pm 0.027 \pm 0.012$	$0.220 \pm 0.024 \pm 0.011$	$0.238 \pm 0.026 \pm 0.012$	$0.252 \pm 0.029 \pm 0.013$	$0.242 \pm 0.033 \pm 0.011$
Pbp					
BackTRACKS	0 13	13 22	22 30	30 47	47 120
prompt	$0.118 \pm 0.008 \pm 0.007$	$0.103 \pm 0.008 \pm 0.006$	$0.106 \pm 0.009 \pm 0.006$	$0.097 \pm 0.008 \pm 0.005$	$0.113 \pm 0.018 \pm 0.006$
from-b	$0.209 \pm 0.032 \pm 0.013$	$0.219 \pm 0.025 \pm 0.012$	$0.217 \pm 0.024 \pm 0.013$	$0.243 \pm 0.023 \pm 0.013$	$0.239 \pm 0.041 \pm 0.013$

B. Fit plots
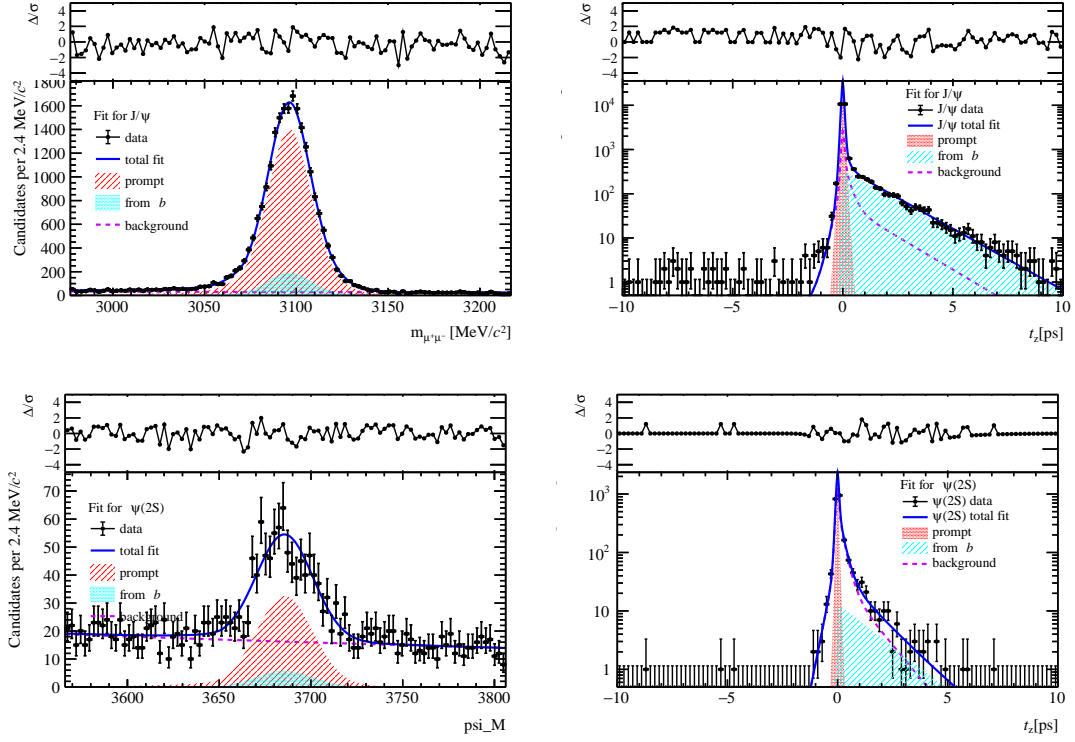
Figure 17: Fit results in $0\,\mathrm{GeV}/c < p_\mathrm{T} < 14\,\mathrm{GeV}/c$, $1.5 < y < 4.5$ and $4\leq$PVNTRACKS<45.
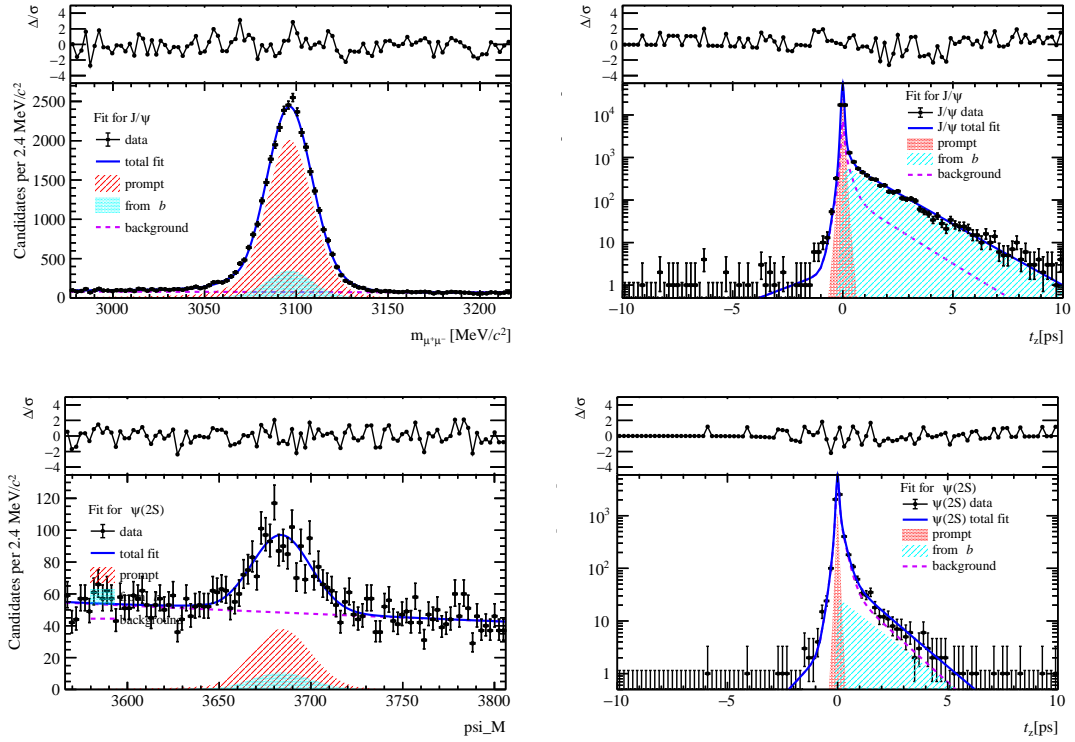
Figure 18: Fit results in $0\,\mathrm{GeV}/c < p_\mathrm{T} < 14\,\mathrm{GeV}/c$, $1.5 < y < 4.5$ and $45\leq$PVNTRACKS<70.
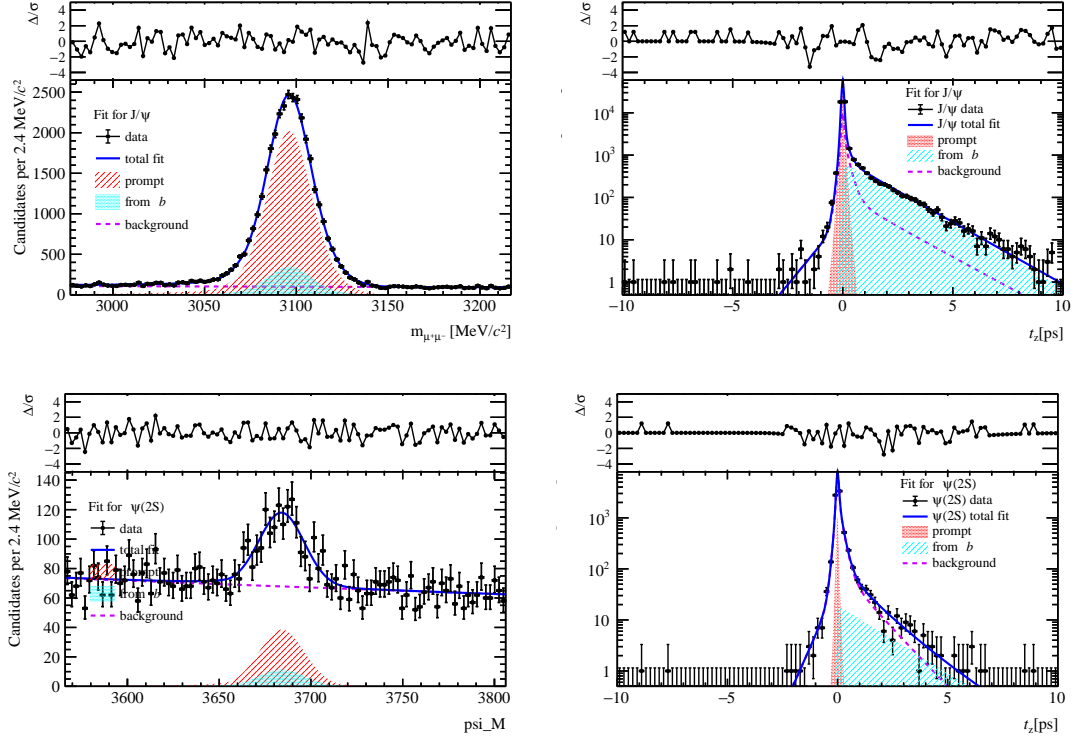
Figure 19: Fit results in $0\,\mathrm{GeV}/c < p_\mathrm{T} < 14\,\mathrm{GeV}/c$, $1.5 < y < 4.5$ and $70 \leq \mathrm{PVNTRACKS} < 90$.
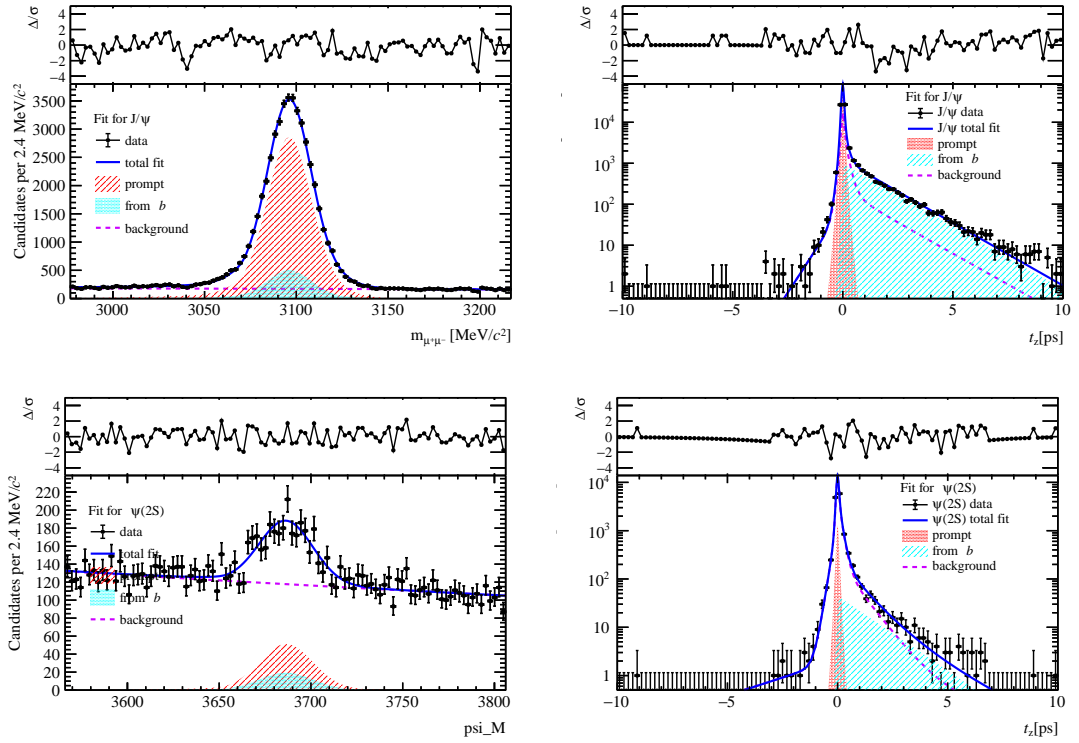
Figure 20: Fit results in $0\,\mathrm{GeV}/c < p_\mathrm{T} < 14\,\mathrm{GeV}/c$, $1.5 < y < 4.5$ and $90 \leq \mathrm{PVNTRACKS} < 120$.
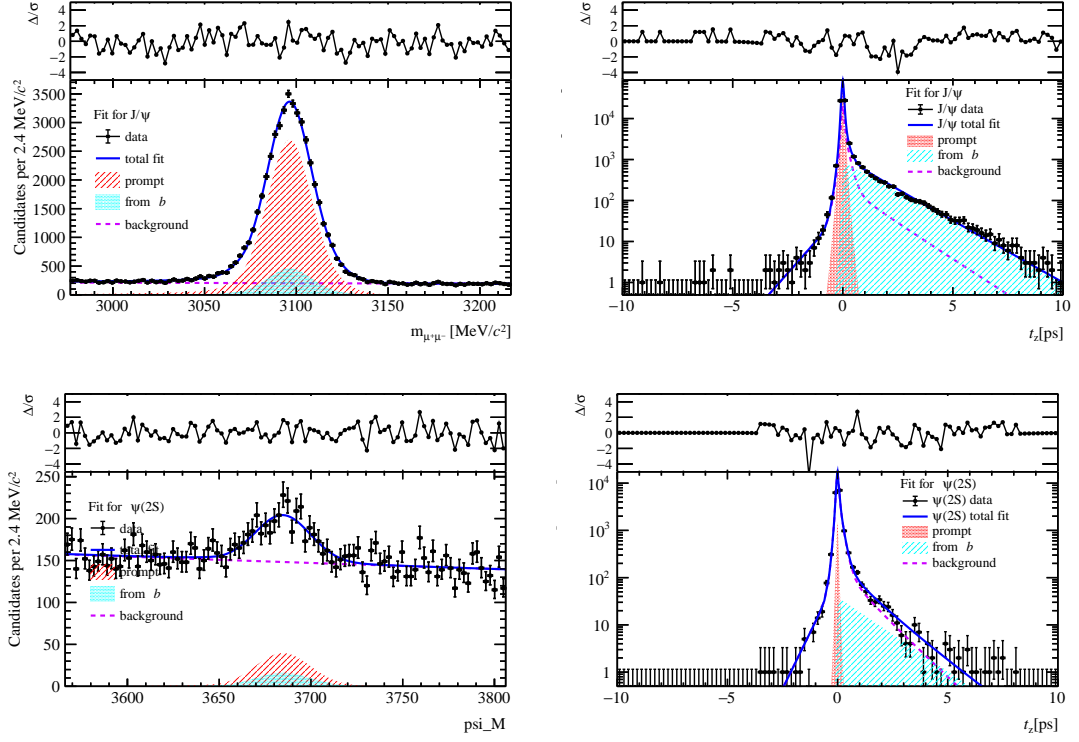
Figure 21: Fit results in $0\,\mathrm{GeV}/c < p_\mathrm{T} < 14\,\mathrm{GeV}/c$, $1.5 < y < 4.5$ and $120{\le}\mathrm{PVNTRACKS}{<}270$.
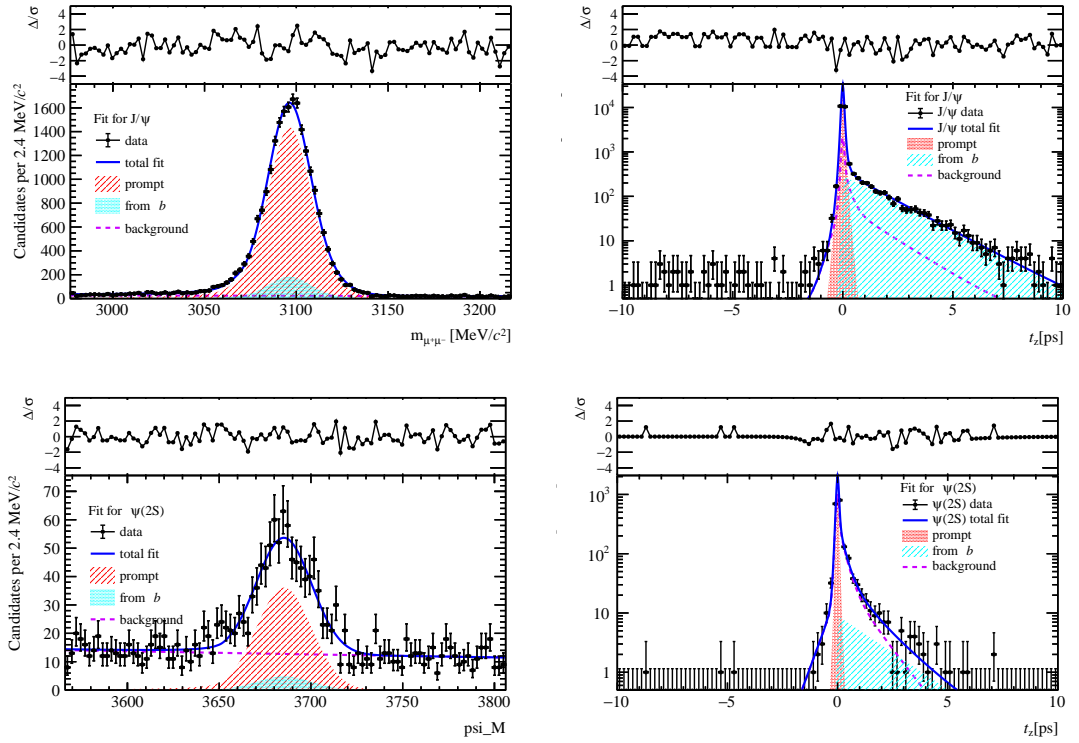
Figure 22: Fit results in $0\,\mathrm{GeV}/c < p_\mathrm{T} < 14\,\mathrm{GeV}/c$, $1.5 < y < 4.5$ and $0{\le}\mathrm{nForwardTracks}{<}25$.
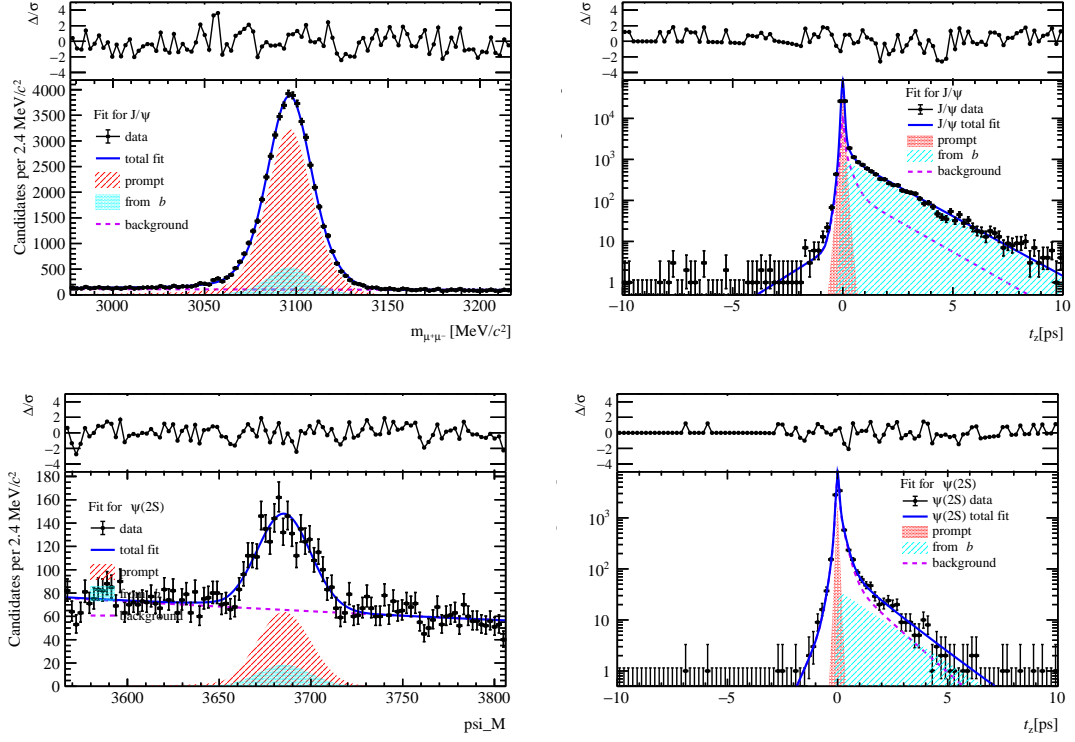
Figure 23: Fit results in $0\,\mathrm{GeV}/c < p_\mathrm{T} < 14\,\mathrm{GeV}/c$, $1.5 < y < 4.5$ and $25 \leq \mathrm{nForwardTracks} < 43$.
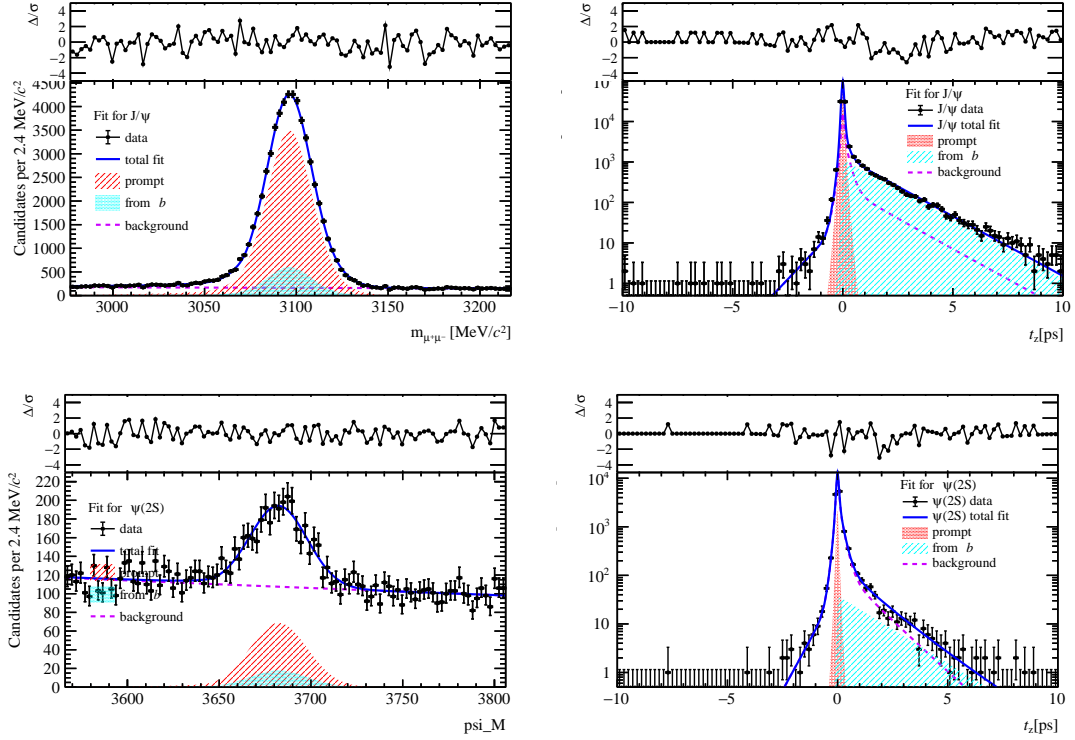
Figure 24: Fit results in $0\,\mathrm{GeV}/c < p_\mathrm{T} < 14\,\mathrm{GeV}/c$, $1.5 < y < 4.5$ and $43 \leq \mathrm{nForwardTracks} < 57$.
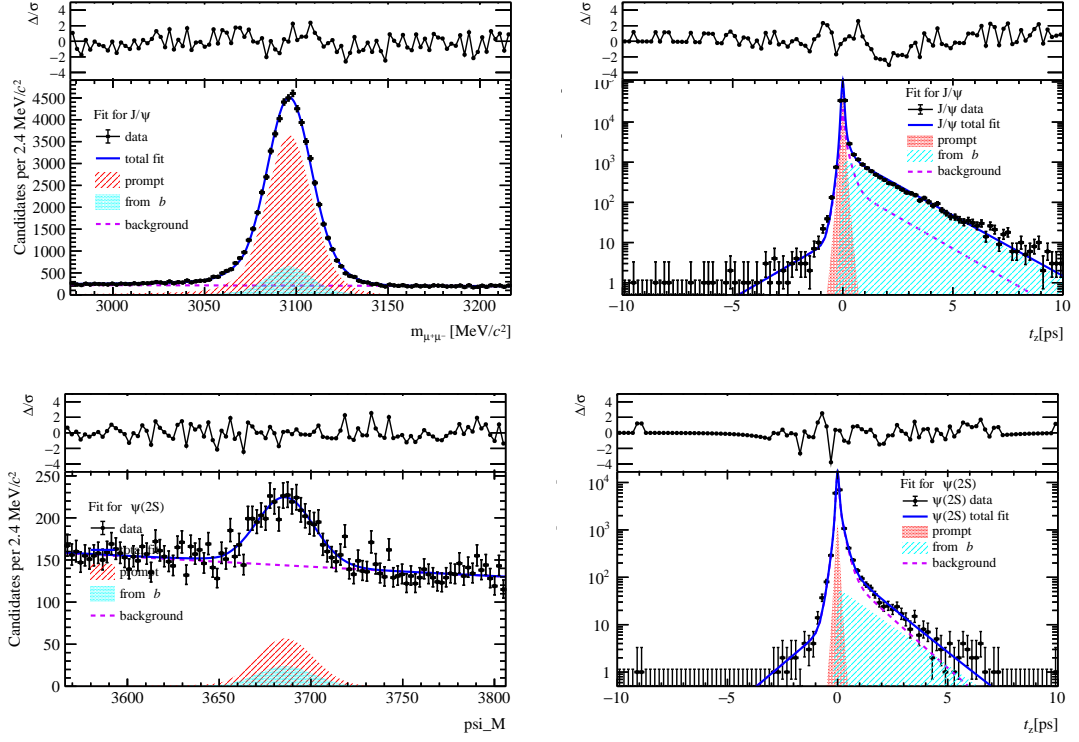
Figure 25: Fit results in $0\,\mathrm{GeV}/c < p_\mathrm{T} < 14\,\mathrm{GeV}/c$, $1.5 < y < 4.5$ and $57 \leq \mathrm{nForwardTracks} < 72$.
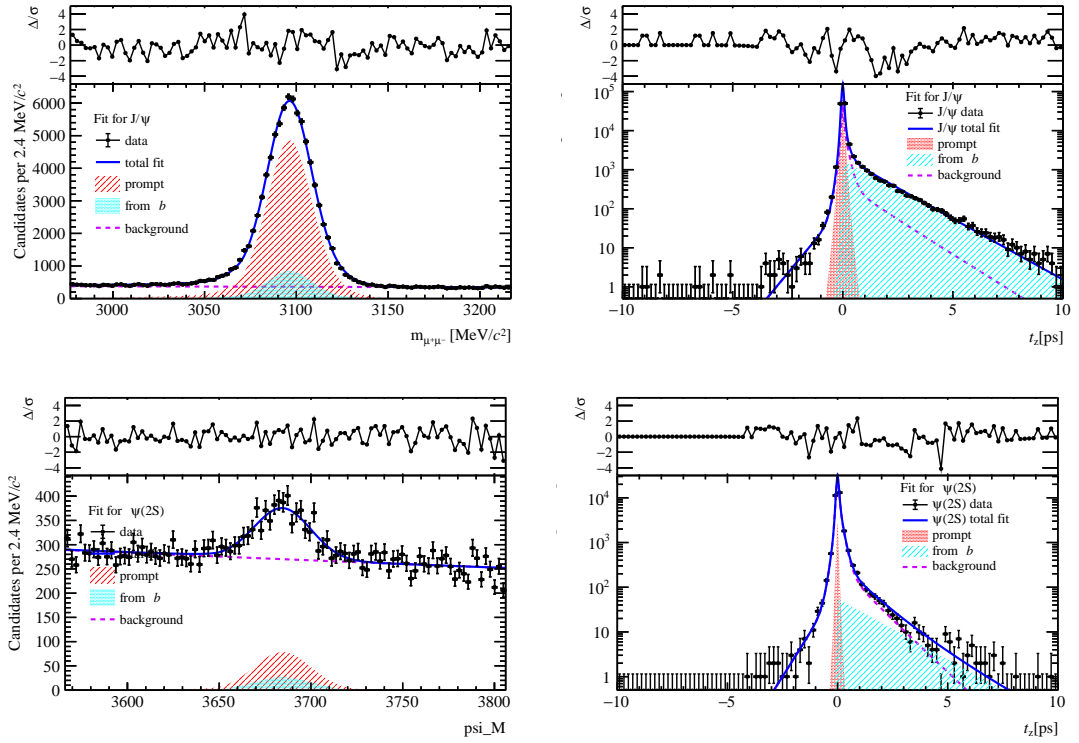
Figure 26: Fit results in $0\,\mathrm{GeV}/c < p_\mathrm{T} < 14\,\mathrm{GeV}/c$, $1.5 < y < 4.5$ and $72 \leq \mathrm{nForwardTracks} < 150$.

33
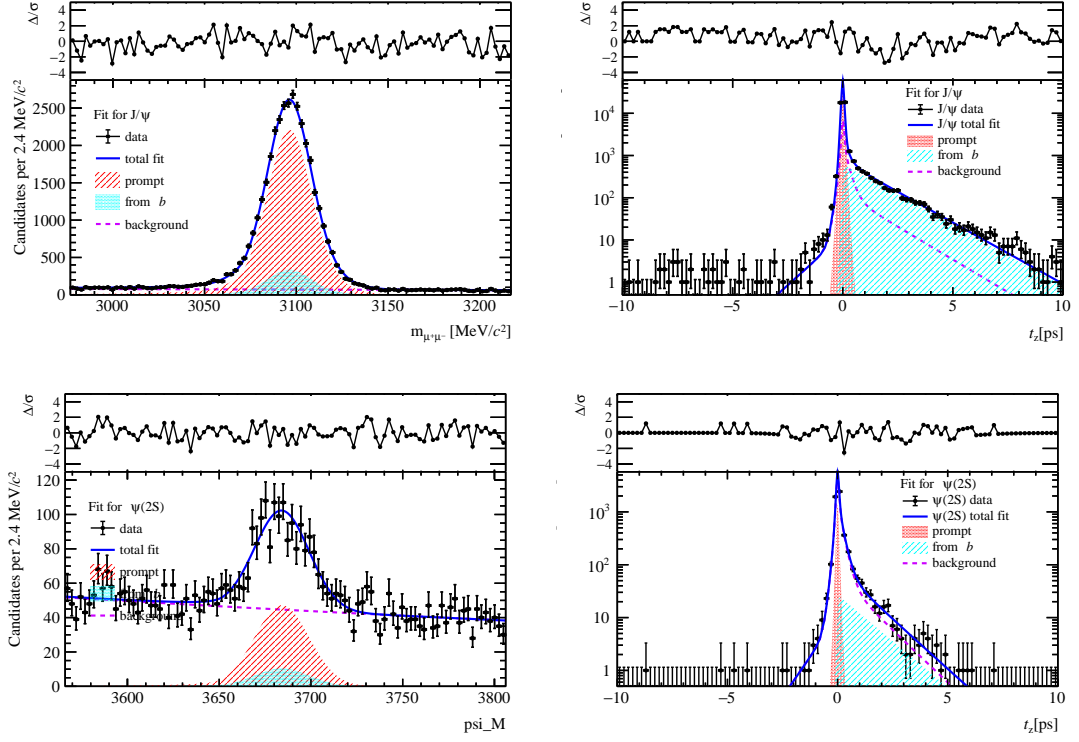
Figure 27: Fit results in $0\,\mathrm{GeV}/c < p_{\mathrm{T}} < 14\,\mathrm{GeV}/c$, $1.5 < y < 4.5$ and $0 \leq$ nBackTracks < 17.
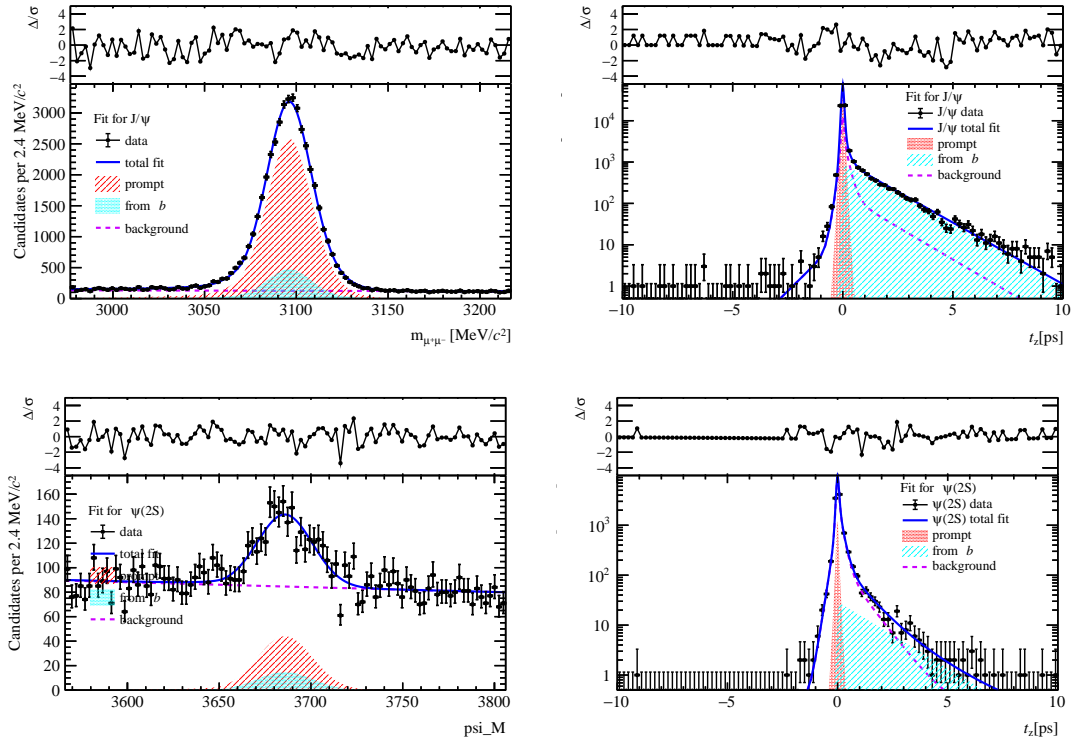
Figure 28: Fit results in $0\,\mathrm{GeV}/c < p_{\mathrm{T}} < 14\,\mathrm{GeV}/c$, $1.5 < y < 4.5$ and $17 \leq$ nBackTracks < 29.
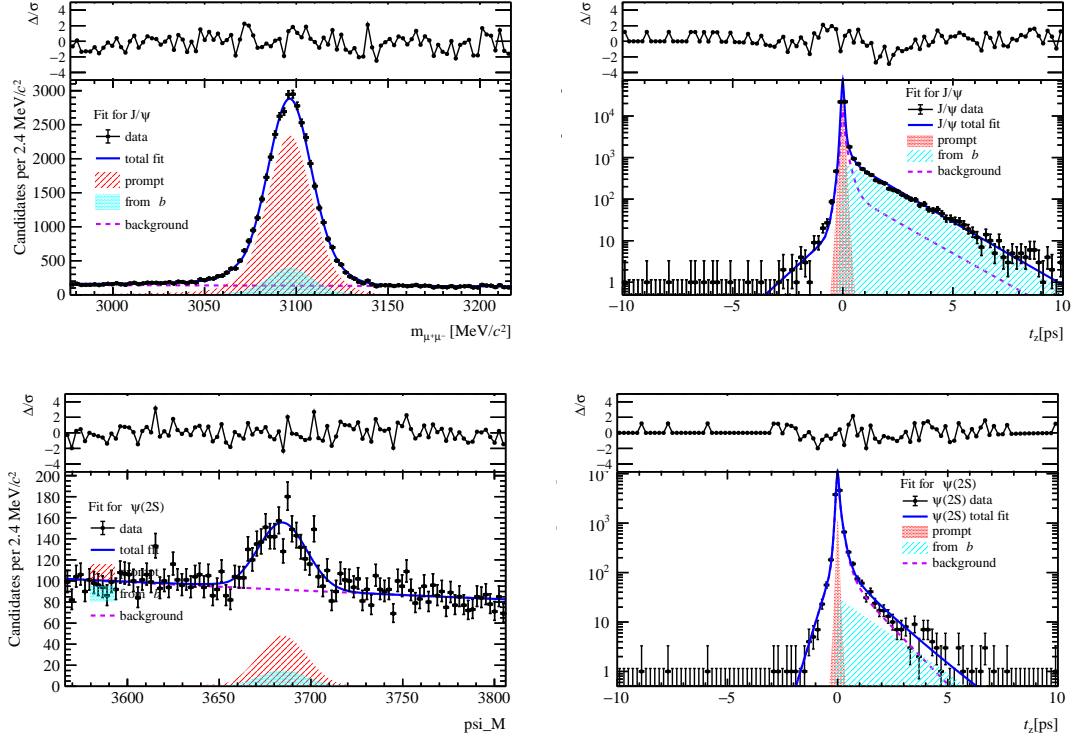
Figure 29: Fit results in $0\,\mathrm{GeV}/c < p_\mathrm{T} < 14\,\mathrm{GeV}/c$, $1.5 < y < 4.5$ and $29 \leq \mathrm{nBackTracks} < 40$.
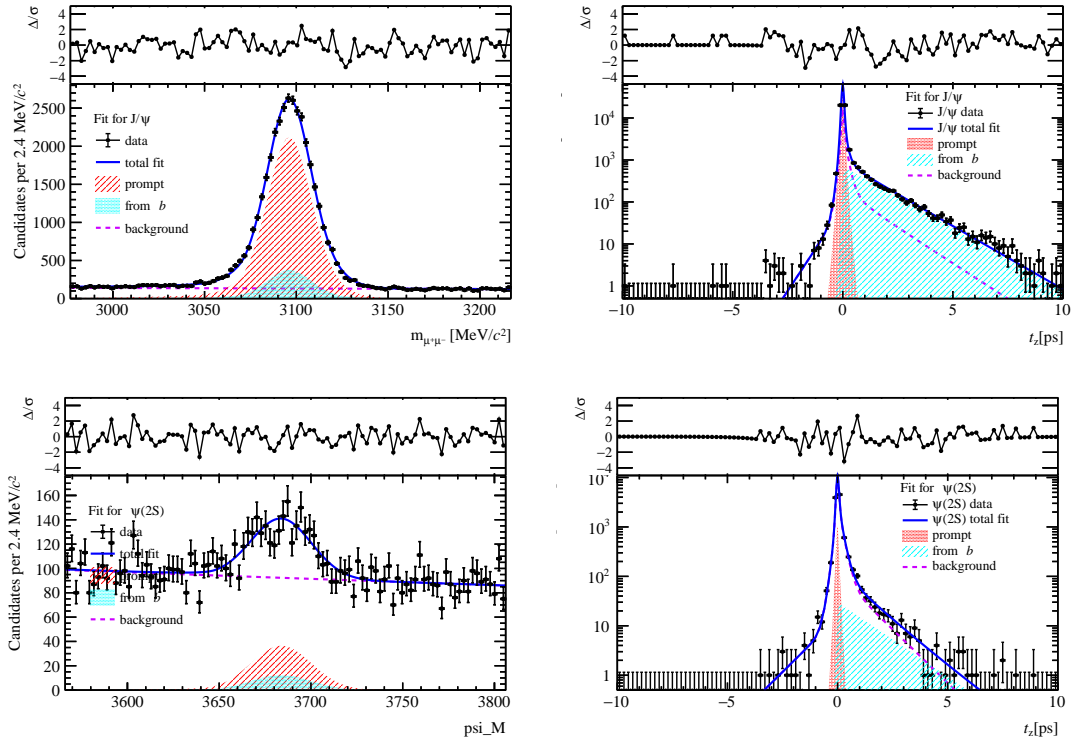
Figure 30: Fit results in $0\,\mathrm{GeV}/c < p_\mathrm{T} < 14\,\mathrm{GeV}/c$, $1.5 < y < 4.5$ and $40 \leq \mathrm{nBackTracks} < 54$.
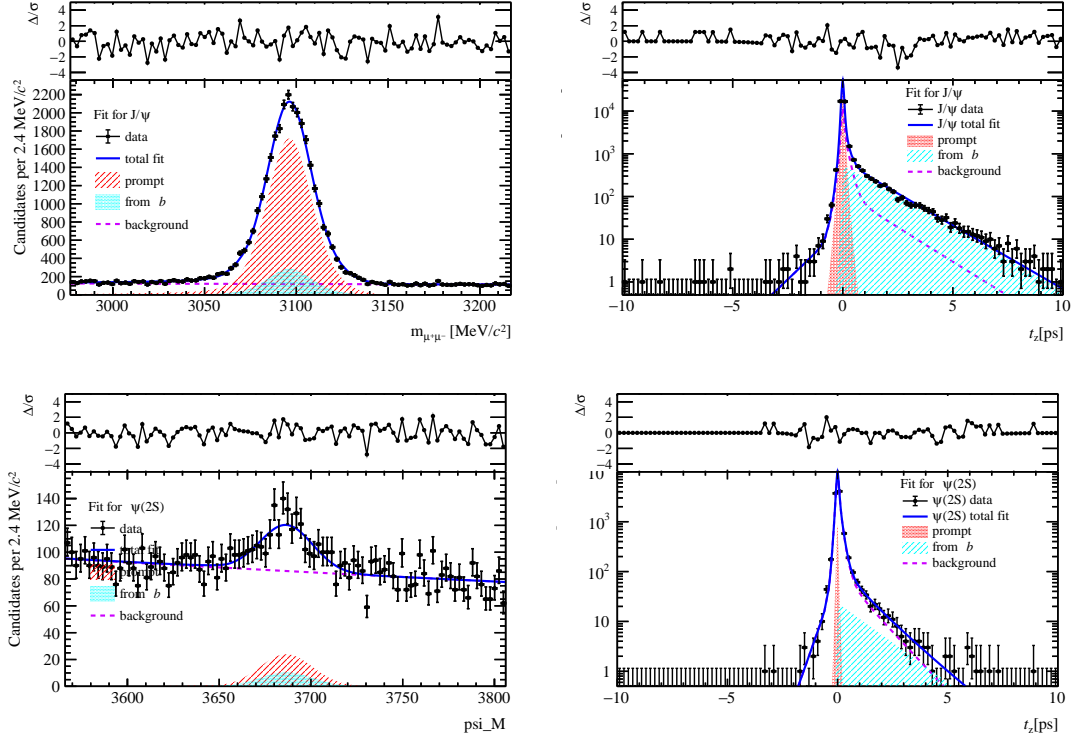
Figure 31: Fit results in $0\,\mathrm{GeV}/c < p_{\mathrm{T}} < 14\,\mathrm{GeV}/c$, $1.5 < y < 4.5$ and $54 \leq \mathrm{nBackTracks} < 180$.

References

[1] H. Satz, *The quark-gluon plasma – a short introduction*, Nuclear Physics A **862-863** (2011) 4.

[2] S. Atashbar Tehrani, *Nuclear parton distribution functions (nPDFs) and their uncertainties in the LHC Era*, KnE Energ. Phys. **3** (2018) 297, arXiv:1712.02153.

[3] F. Arleo and S. Peigné, *Quarkonium suppression in heavy-ion collisions from coherent energy loss in cold nuclear matter*, JHEP **10** (2014) 073, arXiv:1407.5054.

[4] LHCb collaboration, R. Aaij *et al.*, *Study of Υ production in pPb collisions at $\sqrt{s_{NN}} = 8.16$ TeV*, JHEP **11** (2018) 194, arXiv:1810.07655, [Erratum: JHEP 02, 093 (2020)].

[5] ALICE collaboration, S. Acharya *et al.*, *Measurement of nuclear effects on $\psi(2S)$ production in p-Pb collisions at $\sqrt{s_{NN}} = 8.16$ TeV*, JHEP **07** (2020) 237, arXiv:2003.06053.

[6] LHCb collaboration, R. Aaij *et al.*, *Study of $\psi(2S)$ production and cold nuclear matter effects in pPb collisions at $\sqrt{s_{NN}} = 5$ TeV*, JHEP **03** (2016) 133, arXiv:1601.07878.

[7] E. G. Ferreiro, *Charmonium dissociation and recombination at LHC: Revisiting comovers*, Phys. Lett. B **731** (2014) 57, arXiv:1210.3209.

[8] ALICE collaboration, S. Acharya *et al.*, *Centrality dependence of J/ψ and $\psi(2S)$ production and nuclear modification in p-Pb collisions at $\sqrt{s_{NN}} = 8.16$ TeV*, JHEP **02** (2021) 002, arXiv:2008.04806.

[9] CMS collaboration, S. Chatrchyan *et al.*, *Event Activity Dependence of Y(nS) Production in $\sqrt{s_{NN}}=5.02$ TeV pPb and $\sqrt{s}=2.76$ TeV pp Collisions*, JHEP **04** (2014) 103, arXiv:1312.6300.

[10] ALICE collaboration, J. Adam *et al.*, *Enhanced production of multi-strange hadrons in high-multiplicity proton-proton collisions*, Nature Phys. **13** (2017) 535, arXiv:1606.07424.

[11] CMS collaboration, V. Khachatryan *et al.*, *Evidence for collectivity in pp collisions at the LHC*, Phys. Lett. B **765** (2017) 193, arXiv:1606.06198.

[12] CMS collaboration, V. Khachatryan *et al.*, *Observation of Long-Range Near-Side Angular Correlations in Proton-Proton Collisions at the LHC*, JHEP **09** (2010) 091, arXiv:1009.4122.

[13] ALICE collaboration, B. Abelev *et al.*, *Long-range angular correlations on the near and away side in p-Pb collisions at $\sqrt{s_{NN}} = 5.02$ TeV*, Phys. Lett. B **719** (2013) 29, arXiv:1212.2001.

[14] ATLAS collaboration, G. Aad *et al.*, *Observation of Associated Near-Side and Away-Side Long-Range Correlations in $\sqrt{s_{NN}}=5.02$ TeV Proton-Lead Collisions with the ATLAS Detector*, Phys. Rev. Lett. **110** (2013) 182302, arXiv:1212.5198.

[15] LHCb collaboration, R. Aaij *et al.*, *Measurements of long-range near-side angular correlations in* $\sqrt{s_{NN}} = 5\,TeV$ *proton-lead collisions in the forward region*, Phys. Lett. B **762** (2016) 473, arXiv:1512.00439.

[16] S. Agostinelli *et al.*, *Geant4—a simulation toolkit*, Nuclear Instruments and Methods in Physics Research Section A: Accelerators, Spectrometers, Detectors and Associated Equipment **506** (2003) 250.

[17] J. Allison *et al.*, *Geant4 developments and applications*, IEEE Transactions on Nuclear Science **53** (2006) 270.

[18] LHCb collaboration, I. Belyaev *et al.*, *Handling of the generation of primary events in Gauss, the LHCb simulation framework*, J. Phys. Conf. Ser. **331** (2011) 032047.

[19] T. Pierog *et al.*, *EPOS LHC: Test of collective hadronization with data measured at the CERN Large Hadron Collider*, Phys. Rev. C **92** (2015) 034906, arXiv:1306.0121.

[20] D. J. Lange, *The evtgen particle decay simulation package*, Nuclear Instruments and Methods in Physics Research Section A: Accelerators, Spectrometers, Detectors and Associated Equipment **462** (2001) 152, BEAUTY2000, Proceedings of the 7th Int. Conf. on B-Physics at Hadron Machines.

[21] P. Golonka and Z. Was, *PHOTOS Monte Carlo: A precision tool for QED corrections in Z and W decays*, Eur. Phys. J. **C45** (2006) 97, arXiv:hep-ph/0506026.

[22] Particle Data Group, R. L. Workman and Others, *Review of Particle Physics*, PTEP **2022** (2022) 083C01.

[23] LHCb collaboration, R. Aaij *et al.*, *Measurement of forward J/ψ production cross-sections in pp collisions at* $\sqrt{s} = 13\ TeV$, JHEP **10** (2015) 172, arXiv:1509.00771, [Erratum: JHEP 05, 063 (2017)].

[24] J. Lefrancous, *Crystal ball fits*, link.

[25] LHCb collaboration, R. Aaij *et al.*, *Measurement of ψ(2S) production cross-sections in proton-proton collisions at* $\sqrt{s} = 7\ and\ 13\ TeV$, Eur. Phys. J. C **80** (2020) 185, arXiv:1908.03099.

[26] PHENIX collaboration, A. Adare *et al.*, *Measurement of the relative yields of ψ(2S) to ψ(1S) mesons produced at forward and backward rapidity in p + p, p+Al, p+Au, and* $^{3}He+Au$ *collisions at* $\sqrt{s_{NN}} = 200\ GeV$, Phys. Rev. C **95** (2017) 034904, arXiv:1609.06550.

[27] NA50 collaboration, B. Alessandro *et al.*, *J/psi and psi-prime production and their normal nuclear absorption in proton-nucleus collisions at 400-GeV*, Eur. Phys. J. C **48** (2006) 329, arXiv:nucl-ex/0612012.

[28] PHENIX collaboration, A. Adare *et al.*, *Ground and excited charmonium state production in p + p collisions at* $\sqrt{s} = 200\ GeV$, Phys. Rev. D **85** (2012) 092004, arXiv:1105.1966.

[29] E705 collaboration, L. Antoniazzi *et al.*, *Production of J / Psi via psi-prime and xi decay in 300-GeV/c proton and pi+- nucleon interactions*, Phys. Rev. Lett. **70** (1993) 383.

[30] NA51 collaboration, M. C. Abreu *et al.*, *J / psi, psi' and Drell-Yan production in p p and p d interactions at 450-GeV/c*, Phys. Lett. B **438** (1998) 35.

[31] A. G. Clark *et al.*, *Electron Pair Production at the CERN ISR*, Nucl. Phys. B **142** (1978) 29.

[32] UA1 collaboration, C. Albajar *et al.*, *J / psi and psi-prime production at the CERN p anti-p collider*, Phys. Lett. B **256** (1991) 112.

[33] CDF collaboration, F. Abe *et al.*, *J/ψ and $\psi(2S)$ production in $p\bar{p}$ collisions at $\sqrt{s} = 1.8$ TeV*, Phys. Rev. Lett. **79** (1997) 572.

[34] LHCb collaboration, R. Aaij *et al.*, *Exclusive J/ψ and $\psi(2S)$ production in pp collisions at $\sqrt{s} = 7$ TeV*, J. Phys. G **40** (2013) 045001, arXiv:1301.7084.